Research Article

Shabbir Ahmad*, Hidemasa Takana, Kashif Ali, Yasmeen Akhtar, Ahmed M. Hassan, and Adham E. Ragab

Role of localized magnetic field in vortex generation in tri-hybrid nanofluid flow: A numerical approach

https://doi.org/10.1515/ntrev-2022-0561 received March 19, 2023; accepted May 19, 2023

Abstract: Tri-hybrid nanofluid (THNF) can achieve a higher heat transfer rate than conventional hybrid nanofluid by combining three different nanoparticles with synergistic effects. It can have more diverse physical and thermal properties by choosing different combinations of nanoparticles. That is why it has more potential applications in various fields such as solar thermal, biomedical, and industrial processes. On the other hand, vortices are circular motions of liquid or gas that occur when there is a velocity difference. They are important for understanding how fluids mix and transport mass. They can be found in nature, such as in tornadoes and hurricanes. The aim of the current study is to mainly investigate the complex interaction of Lorentz force with the tri-hybrid nanoparticles inside a lid-driven square cavity. It can be seen that the magnetic field has caused the evolution of new vortices (which are very important while analyzing any flow model due to their importance in interpreting fluid mixing and mass transport phenomena) in the flow field, thus adding much more significance to our work. Most of the scientific literature is enriched with investigations dealing with the problems assuming a uniform magnetic field occupying the flow field, but in this research, a vertical strip of magnetism within the flow field will be introduced. It may be the first effort to interpret the role of the applied magnetic field in the formation of the new vortices in the flow field. A single-phase model is utilized to describe THNF whereas a numerical solution to the governing differential equations has been obtained by employing an algorithm based on the central difference discretization and the alternating direction implicit method. The analysis reveals that the magnetic field intensity may result in up to 13 and 119% increase in the skin friction and Nusselt number, respectively. Similarly, a remarkable change in the Nusselt number and the skin friction is also observed by raising the Reynolds number Re. Moreover, the localization or confinement of the magnetic field does not always increase or decrease the Nusselt number. Thus, it is concluded that there will be a certain width of the magnetic corridor for which the Nusselt number would be optimal. Further, the THNF containing Al₂O₃, Ag, and TiO₂ outperforms in terms of enhancing the average Nusselt number, compared to the simple nanofluid containing the abovementioned particles.

Keywords: Reynolds number, single-phase model, tri-hybrid nanofluids, localized magnetic field

Hidemasa Takana: Institute of Fluid Science, Tohoku University, Sendai 980-8577, Japan

Kashif Ali: Department of Basic Sciences and Humanities, Muhammad Nawaz Sharif University of Engineering and Technology, Multan 60000, Pakistan

Yasmeen Akhtar: College of Pharmaceutical Sciences, Zhejiang University, Hangzhou 310030, China

Ahmed M. Hassan: Faculty of Engineering, Future University in Egypt, New Cairo, Egypt

Adham E. Ragab: Department of Industrial Engineering, College of Engineering, King Saud University, P.O. Box 800, Riyadh 11421, Saudi Arabia

Nomenclature

Eckert number Ec $\tilde{H}(x, y)$ magnetic field intensity of a dipole K pyro magnetic factor Ñ magnetization property Mn magnetic number Pr Prandtl number Re Reynolds number \bar{T}_{c} Curie temperature constant velocity V_0 $\partial \tilde{H}/\partial x$ magnetic force components along the X-axis $\partial \tilde{H}/\partial y$ magnetic force components along the Y-axis

^{*} Corresponding author: Shabbir Ahmad, Institute of Geophysics and Geomatics, China University of Geosciences, Wuhan 430074, China; Department of Basic Sciences and Humanities, Muhammad Nawaz Sharif University of Engineering and Technology, Multan 60000, Pakistan, e-mail: shabbiraleem@cug.edu.cn

Greek symbols

 γ magnetic field strength $\mu_{\rm hnf}$ viscosity of hybrid nanofluid

 σ_{hnf} electrical conductivity of hybrid nanofluid

 $\widehat{\varphi}_1$ volume fraction of iron oxide

 $\widehat{\rho}_{\rm nf}$ density of nanofluid

nanoparticle volume fraction

 $egin{array}{ll} arepsilon & ext{dimensionless number} \\ ar{\mu}_0 & ext{dynamic viscosity} \\ k_{ ext{hnf}} & ext{thermal conductivity} \\ \widehat{arphi}_2 & ext{volume fraction of copper} \end{array}$

 $\widehat{
ho}_{
m hnf}$ density of nanofluid of hybrid nanofluid

1 Introduction

The study of vortex generation in lid-driven cavities by localized magnetic field is useful for understanding the fluid dynamics of biological fluids under the influence of high magnetic fields and its possible medical applications, such as cell separation, magnetic tracers, and magnetic drug targeting [1]. It is also useful for exploring the sizedependent effects of fluid flows at small scales, which can be relevant for liquid crystals, lubrication, and microelectromechanical devices [2]. Moreover, it can provide insights into the topology and stability of corner vortices in the liddriven cavity flow, which is a benchmark problem for testing numerical methods and studying fundamental aspects of incompressible flows in confined volumes [3]. A localized magnetic field is a vector field that varies in space due to the presence of magnetic materials or electric currents. Some real-world applications of localized magnetic fields are indoor localization, magnetic anomaly detection, magnetoencephalography, and quantum physics. Magnetic fields can be used to estimate the position and orientation of a device inside a building by measuring the distortions of the earth's magnetic field caused by ferromagnetic objects [4,5].

Amalgamation of the nanoparticles that are exhibiting magnetic features may produce magnetic nanofluids which are rather different from ordinary nanofluids. Since ferromagnetic materials such as ferrites, mercury, and nickel are likely more striking towards the influence of the external magnetic fields, these nanomaterials disseminate the fluid throughout the enclosure by altering the flow regime. In a magnetic field setup, the flow of viscous and conductive fluids (e.g., Brine, nano lubricants, plasma, electrolytes, liquid metals, etc.) has a variety of applications in the manufacturing of medical apparatuses, control networks in

industries, propulsion systems in submarine and spacecraft, wastewater treatment, liquid metal fast reactor, power generation, etc. In recent times, many researchers have focused on magneto-hydrodynamic (MHD) flows through different geometries. Recently, the heat and mass transfer of a microrotating fluid between two plates was explored by Jalili et al. [6] by using both electric and magnetic fields. They computed the nonlinear and coupled equations and evaluated how the Nusselt number, Sherwood number, and skin friction influence the fluid's temperature, concentration, and velocity. MHD convection and the development of entropy of Cu-Al₂O₃/water nanofluid in a porous square cavity are numerically investigated with sinusoidal boundary temperatures by Abdel-Nour et al. [7]. The isotherms vary with Rayleigh number and Hartmann number (Ha). A high Ha increases conduction transfer. MHD mixed convection in Al₂O₃-Cu nanostructures in the water nanofluid in an L-shaped cavity with two heat sources at bottom corners and cold ends is proposed by Armaghani et al. [8]. The size of the enclosure and heat source location affect the heat transfer and flow. The numerical study of unsteady hybrid nanofluid (Fe₃O₄ and carbon nanotubes in water) flow with heat source/sink effects between two sheets with variable thermal conductivity and magnetic field has been conducted by Dinarvand et al. [9]. The heat transfer decreases with an oblique magnetic field and also temperature-dependent thermal conductivity. The spherical particles have a particularly high temperature with horizontal magnetic field.

Convective flows through enclosures and cavities have captivated the attention of scientists due to their increasingly versatile applications in several industries which include chemical and food processing industries, paints and molten polymer processing units, microelectronics, HVAC systems of buildings and mechanical complexes, nuclear power stations, solar collectors, etc. [10-12]. Natural convection flow problems are mainly concerned with the heat transfer performance of the working fluids. Fluid flow and heat transfer in a square cavity with varying wall temperatures and Cu-Al₂O₃water nanofluid is numerically investigated by Gorla et al. [13]. A higher Ha lowers fluid velocity and a higher nanoparticle volume fraction boosts the heat transfer rate. The heat transfer of a hybrid nanofluid in a triangular cavity with a magnetic field and a heat source at the bottom is studied by Rashad et al. [14]. The slanted side is cold and the other sides are insulated. The heat transfer is affected by the nanofluid volume fraction when convection is very low. A hybrid nanofluid with an equal nanostructure of copper (Cu) and aluminum oxide (Al₂O₃) in water does not improve the mean Nusselt number more than a regular nanofluid. Excellent research

on the thermophysical characteristics of various nanofluids in fascinating problems was also conducted by Ahmad et al. [15-22]. Liu et al. [23] examined the magnetic flow of Fe₃O₄ nanoparticles inside a porous cavity with the latest numerical technique taking impacts of various combinations of Rayleigh numbers, the volume fraction of nanocomposites, porosity parameter, and magnetic parameters on the thermal distributions of the nano liquid. Nepal [24] calculated a numerical solution of MHD flow through an enclosure with numerous heat sources of variable breadth at the bottom most layer of the enclosure. The author employed a powerful numerical technique, the successive over-relaxation method, entrenched with relevant finite differences of differential equations.

The advantage of tri-hybrid nanofluids (THNFs) over hybrid nanofluids is that they have higher thermal conductivity and heat transfer properties than hybrid nanofluids and simple nanofluids [25,26]. This means that THNFs can enhance the cooling performance and energy efficiency of various applications, such as microfluidic devices, electric ovens, nuclear reactors, etc. However, the effectiveness of THNFs depends on several factors, such as the types, sizes, shapes, and mixture ratios of nanoparticles, as well as the base fluids [27]. Jakeer et al. [28] studied the magneto copper based nanofluid flow in a non-Darcy porous square enclosure by using the Cattaneo-Christov heat flux model. The heat transfer and flow depend on the heated obstacle. Higher Ha reduces the local Nusselt number, whereas hybrid nanofluid enhances heat transfer more than nanofluids. The thermal diffusivity profile in oblique stenosis artery with Al₂O₃–Cu based hybrid nanofluid was designed by Jalili et al. [29] by taking care of several numerical methods (AGM, FEM, and Runge-Kutta). They scrutinized the influence of heat source parameters and volume fraction on the temperature evolution and reported that increasing the nanoparticles volume fraction decreases the maximum temperature profile and rising the heat source increases the maximum heat temperature. They also discovered that Al₂O₃ has more impact on reducing the temperature profile than Cu. The best cooling of the fluid was accomplished by Abdollahi et al. [30] by perusing the thermal and fluid parameters of copper/water hybrid solution, such as Darcy number and Nusselt number. They also fitted a piece of fin on the wall of the heat sink to surge the coefficient of displacement heat transfer and conductive heat transfer with the surrounding air-fluid and the effectiveness of the system. Tawade et al. [31] examined the steady laminar flow on a two-dimensional boundary layer with heat transfer of Casson over a linearly stretching sheet. The governing partial differential equations (PDEs) were changed into nonlinear ordinary differential equations

(ODEs) by means of similarity transformation. For more related information, please refer to refs [32,33]. Hameed et al. [34] studied the two-dimension flow of Casson hybrid nanofluid on a nonlinear extending surface with a magnetic field, absorption, heat generation, and viscous dissipation. The main aim is to enhance the heat transfer relationship between the engineering industries and manufacturing.

In most recent times, various nanoparticles such as alumina, titanium, spinel ferrites, nickel, copper, silver, graphite, etc., are used in the working host fluids to produce thermally vigorous fluids usually termed nanofluids [35–38]. The study of a micro-polar nanofluid in a rotating system with electric and magnetic fields between two plates was conducted by Jalili et al. [39]. They considered a steady-state fluid flow and integrated the coupled and nonlinear equations with appropriate similar variables, and employed new semi-analytical and numerical methods to define the accuracy of the results. They reported that concentration value decays by increasing the thermophoretic parameter and Reynolds number. Heat transfer and entropy generation in a square enclosure with aluminum and copper based nanofluid at different wall temperatures associated with imposed magnetic field are studied by Mansour et al. [40]. A new semi-analytical technique was used by Jalili et al. [41] to crack the heat and mass transfer problem. They considered a viscous, laminar axisymmetric, and incompressible flow of a micropolar fluid under the effect of a magnetic field between two stretchable disks. They presented the impact of different parameters such as radiation parameter, Eckert number, magnetic field, Reynolds number, Prandtl number, and Schmidt number on the profiles of microrotation, temperature, velocity, and concentration with the corresponding graphs. Saeed et al. [42] explored the complex dynamics of nanofluid flow between two parallel plates that squeeze and rotate with various physical properties. They used the Navier-Stokes equation, energy equation, and concentration equation to model the unsteady behavior of the fluid and its thermal and mass transport characteristics. The problem of variable viscosity and inclined Lorentz force influences on Williamson nanofluid on a stretching plate was unraveled by Jalili et al. [43] by considering a semianalytical approach. The variable viscosity was chosen to change with temperature as a linear function. The system of PDEs was transformed into ODEs using suitable transformations. The outcomes demonstrated that the heat transfer rate reduced by increasing the Prandtl number and the temperature decreased by rising the thermophoresis parameter.

One of the imperative problems of heat transfer through bounded surfaces is natural convection, in which the governing equations are highly nonlinear and coupled in nature, and require advanced computational fluid dynamics tools to obtain their numerical solutions. Yuan et al. [44] numerically solved the hydromagnetic flow of nano liquid inside a U-shaped cavity. In order to prevent the bafflement on the fluid movement inside the enclosure, clockwise and anti-clockwise vortices are observed at greater scales of Rayleigh number. The convection heat transfer in a turbulent flow in a countercurrent doubletube heat exchanger with various fins was investigated by Jalili et al. [45]. The double-pipe heat exchanger was studied for the real cooling or heating process of fluids. Water-titanium dioxide and water-aluminum oxide nanofluids at quatern concentrations (0.4, 2, 4, and 6%) were considered as the cold fluid in the innermost tube, and water as the hot fluid in the annular space. The findings indicated that the $Al_2O_3 + H_2O$ nanofluid had an improved convection heat transfer coefficient than TiO₂ + H₂O and pure water. A numerical model of a shell and tube heat exchanger associated with non-continuous helical baffles (NCHB-STHX) was investigated by Jalili et al. [46]. This heat exchanger has miscellaneous applications in different arenas of science and industry. They subjugated the ratio of heat transfer coefficient to pressure drop (HTC/ ΔP) from various angles and intensities. Dharmaiah *et al.* [47] analyzed the behavior of nanofluid flows through a sinusoidally varying circular cylinder numerically by applying the

similarity transformations which reduce the governing equations to nonlinear ODEs. Sherwood number, Skin friction, and Nusselt number are also evaluated with the use of bvp4c. Dharmaiah *et al.* [48] considered an incompressible non-Newtonian nanofluid in a two-dimensional transitory boundary layer through a cone. The radiation absorption and Arrhenius activation energy are taken into account by the non-Newtonian nanofluid model. The nonlinear equations are numerically solved using ODE45 MATLAB bvp4c and the Runge–Kutta integration method. Skin friction is reduced when the activation energy parameter is higher, while Nusselt and Sherwood values are increased.

The novelty or originality of the study lies in the combination of lid-driven cavity flow, localized magnetic field, and THNFs, which introduce additional boundary conditions. A vertical strip of magnetism will be introduced within the flow field and its impact on the flow characteristics will be observed. The work under consideration may be the first effort to interpret the role of the applied magnetic field in the formation of the new vortices in the flow field. The work mainly aims to investigate the complex interaction of Lorentz force with the tri-hybrid nanoparticles inside a lid-driven square cavity. Lorentz force causes the spinning of the nano-sized hybrid particles and thus generates a complicated structure of vortices.

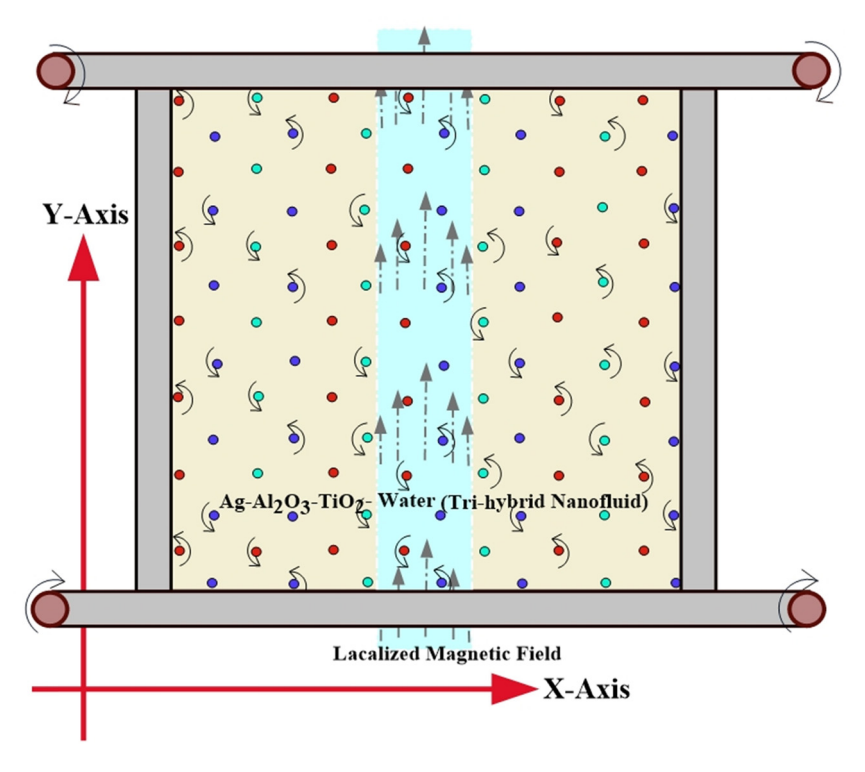


Figure 1: Schematic illustration of the problem.

2 Problem description

The schematic representation of the two-dimensional square enclosure taken into consideration is depicted in Figure 1. The physical domain of a square with side L. A localized magnetic field is constantly embedded in the lower horizontal wall. A single-phase model is being used to build the governing equations for a two-dimensional enclosure.

2.1 Basic assumptions

• A magnetic source creates the magnetic field with intensity H, as given by

 $\tilde{H}(x, y) = H_0 \{ \tanh A'_1(x - x_1) - \tanh A'_2(x - x_2) \}, \text{ in }$ the strip defined by $x_1 \le x \le x_2$, and $0 \le y \le L$.

- · Both vertical walls are insulated, whereas the enclosure's top and bottom horizontal walls are kept at a constant temperature.
- Lower and upper horizontal walls slide uniformly from left to rightward with a constant velocity V_0 .
- · Newtonian, incompressible, and laminar nanofluids are assumed in the current analysis.
- The solid nanoparticles (silver; Ag, aluminum oxide; Al₂O₃, and titanium dioxide; TiO₂), and the base fluid (water) are in thermal equilibrium.
- The thermo-physical parameters of the nanofluid are taken to be constant.

3 Governing equations and dimensionless variables

The basic laws, assumptions, and derivation of the Navier-Stokes equations are based on the following principles:

- The fluid is a continuum, i.e., it is treated as a continuous substance rather than discrete particles.
- The fluid is incompressible, i.e., its density is constant and independent of pressure [49].
- The fluid is Newtonian, i.e., its stress is proportional to its strain rate [49].
- The fluid obeys the conservation of mass, i.e., the mass of a fluid element does not change as it moves.
- The fluid obeys the conservation of momentum, i.e., the net force acting on a fluid element is equal to its rate of change of momentum.
- The fluid obeys the conservation of energy, i.e., the net work done on a fluid element is equal to its rate of change of energy

The dimensional form of these equations is as follows [50]:

Continuity equation

$$\frac{\partial \tilde{U}}{\partial x} + \frac{\partial \tilde{V}}{\partial y} = 0, \tag{1}$$

Momentum equation

$$\frac{\partial \tilde{U}}{\partial t'} + \left(\tilde{V} \frac{\partial \tilde{U}}{\partial y} + \tilde{U} \frac{\partial \tilde{U}}{\partial x} \right) \\
= -\frac{1}{\widehat{\rho_{\text{thnf}}}} \frac{\partial P}{\partial x} + \widehat{v_{\text{thnf}}} \left(\frac{\partial^2 \tilde{U}}{\partial y^2} + \frac{\partial^2 \tilde{U}}{\partial x^2} \right) + \frac{\bar{\mu}_0 \tilde{M}}{\widehat{\rho_{\text{thnf}}}} \frac{\partial \tilde{H}}{\partial x}, \tag{2}$$

$$\frac{\partial \tilde{V}}{\partial t'} + \left(\tilde{U} \frac{\partial \tilde{V}}{\partial x} + \tilde{V} \frac{\partial \tilde{V}}{\partial y} \right) \\
= -\frac{1}{\widehat{\rho}_{thmf}} \frac{\partial P}{\partial y} + \widehat{U}_{thmf} \left(\frac{\partial^2 \tilde{V}}{\partial x^2} + \frac{\partial^2 \tilde{V}}{\partial y^2} \right) + \frac{\overline{\mu}_0 \tilde{M}}{\widehat{\rho}_{thmf}} \frac{\partial \tilde{H}}{\partial y}, \tag{3}$$

Energy equation

$$\frac{(\widehat{\rho} c_{p})_{thnf}}{k_{thnf}} \left[\widetilde{U} \frac{\partial T}{\partial x} + \widetilde{V} \frac{\partial T}{\partial y} \right] + \left[\frac{\overline{\mu}_{o}}{k_{thnf}} \right] T \frac{\partial \widetilde{M}}{\partial T} \left[\widetilde{V} \frac{\partial \widetilde{H}}{\partial y} + \widetilde{U} \frac{\partial \widetilde{H}}{\partial x} \right] \\
= \nabla^{2} T + \left[\frac{\widetilde{\mu}_{thnf}}{k_{thnf}} \right] \left[2 \left[\frac{\partial \widetilde{U}}{\partial x} \right]^{2} + \left[\frac{\partial \widetilde{V}}{\partial x} + \frac{\partial \widetilde{U}}{\partial y} \right]^{2} + 2 \left[\frac{\partial \widetilde{V}}{\partial y} \right]^{2} \right]. \tag{4}$$

It is to point out that the energy equation is based on the following energy balance:

The time rate of change of energy in a system at time t =[The net rate of heat transfer into a system at time t] – [The net rate of work out of a system at time t].

In the above equations,

$ar{\mu}_0 ilde{M} rac{\partial ilde{H}}{\partial x}$	Magnetic force component along the <i>X</i> -axis	$\bar{\mu}_0 \tilde{M} \frac{\partial \tilde{H}}{\partial y}$	Magnetic force component along the <i>Y</i> -axis
$\bar{\mu}_0 T \frac{\partial \tilde{M}}{\partial T} \left[\tilde{U} \frac{\partial \tilde{H}}{\partial x} + \tilde{V} \frac{\partial \tilde{H}}{\partial y} \right]$	Magneto- caloric phenomenon	γ	Magnetic field strength
$\tilde{M} = K\tilde{H}(\bar{T}_{\rm c} - T)$	Magnetization property	$\overline{T}_{ m c}$	Curie tem- perature [51]
$\frac{\partial \tilde{U}}{\partial t'} + \left(\tilde{V} \frac{\partial \tilde{U}}{\partial y} + \tilde{U} \frac{\partial \tilde{U}}{\partial x} \right)$	Convection terms	$\left(\frac{\partial^2 \tilde{U}}{\partial y^2} + \frac{\partial^2 \tilde{U}}{\partial x^2}\right)$	Diffusion terms
$\frac{\partial \tilde{V}}{\partial t'} + \left(\tilde{U} \frac{\partial \tilde{V}}{\partial x} + \tilde{V} \frac{\partial \tilde{V}}{\partial y} \right)$	Convection terms	$\left(\frac{\partial^2 \tilde{U}}{\partial y^2} + \frac{\partial^2 \tilde{U}}{\partial x^2}\right)$	Diffusion terms

It is important to keep in mind that the subscript (hnf) is used to indicate the physical properties of a THNF.

It is important to keep in mind that convection terms refer to the terms in the equations on the left side of the

momentum equations. Convection is a physical phenomenon that takes place in a gas flow in which the ordered movement of the flow transports some property. The diffusion terms are those on the right-hand side of the momentum equations which are multiplied by the inverse Reynolds number. Diffusion is a physical process that occurs in a flow of gas and involves the random motion of the gas molecules transporting some property. The stress tensor and the viscosity of the gas are related to diffusion. Diffusion in the flow causes turbulence and the formation of boundary layers.

Eliminating the pressure term results in

$$\frac{\partial}{\partial t'} \left(\frac{\partial \tilde{U}}{\partial y} - \frac{\partial \tilde{V}}{\partial x} \right) + \widehat{V} \frac{\partial}{\partial y} \left(\frac{\partial \tilde{U}}{\partial y} - \frac{\partial \tilde{V}}{\partial x} \right)
+ \widetilde{U} \frac{\partial}{\partial x} \left(\frac{\partial \tilde{U}}{\partial y} - \frac{\partial \tilde{V}}{\partial x} \right)
= \widehat{v}_{thnf} \left(\frac{\partial^{2}}{\partial x^{2}} + \frac{\partial^{2}}{\partial y^{2}} \right) \left(\frac{\partial \tilde{U}}{\partial y} - \frac{\partial \tilde{V}}{\partial x} \right)
+ \left(\frac{\partial \left(\frac{\overline{\mu}_{0} \tilde{M}}{\widehat{\rho}_{thnf}} \frac{\partial \tilde{H}}{\partial x} \right)}{\partial y} - \frac{\partial \left(\frac{\overline{\mu}_{0} \tilde{M}}{\widehat{\rho}_{thnf}} \frac{\partial \tilde{H}}{\partial y} \right)}{\partial x} \right).$$

3.1 Boundary conditions

The current problem's dimensional boundary conditions are interpreted as follows:

Left and right walls (Adiabatic)

$$\left(\frac{\partial T}{\partial x}\right)_{x=0} = 0, \left(\frac{\partial T}{\partial x}\right)_{x=L} = 0, \ \tilde{U}(0, y) = \tilde{V}(0, y)
= \tilde{U}(L, y) = \tilde{V}(L, y) = 0, \ 0 < y < L,$$
(6a)

Top wall

$$\tilde{U}(x, L) = V, \tilde{V}(x, L) = 0, T(x, L) = T_c; 0 < x < L,$$
 (6b)

Bottom wall

$$\tilde{U}(x, 0) = V, \tilde{V}(x, 0) = 0, T(x, 0) = T_h; 0 < x < L.$$
 (6c)

3.2 Thermophysical characteristics of THNFs

To look into the features of THNFs' heat transport, a particular combination of thermophysical parameters for Al_2O_3 –Ag– TiO_2 tri-hybrid nanoparticles is taken into account. These thermophysical characteristics were derived and validated from the published literature [52]. Below is a description of each symbol that appears in Table 1.

The formulas suggested in the literature can be used to analyze the thermophysical characteristics of a THNF.

The following set of dimensionless variables should be used right now:

$$\xi = \frac{x}{\widehat{L}}, \ y = \frac{y}{\widehat{L}}, \ u = \frac{\widetilde{U}}{v_0}, \ v = \frac{\widetilde{V}}{v_0}, \ \widehat{\theta} = \frac{T - T_c}{\Delta T},$$

$$H = \frac{\widetilde{H}}{H_0}, \ t = \frac{v_0}{\widehat{L}}t'.$$
(7)

Now equations (4) and (5) imply that

	For THNFs	For hybrid For For base fluids nanofluids (water)	For solid				
			(water)	Aluminum oxide (s ₁)	Silver (s ₂)	Titanium dioxide (s ₃)	
Viscosity	$\mu_{ m thnf}$	$\mu_{ m hnf}$	$\mu_{ m nf}$	$\mu_{ m f}$			
Density	$\widehat{ ho_{ m thnf}}$			$\widehat{ ho_{ m f}}$	$\widehat{ ho_{\!\!\scriptscriptstyle m S1}}$	$\widehat{ ho_{\!\!\scriptscriptstyle \mathrm{S}2}}$	$\widehat{ ho_{\!_{ m S3}}}$
Electrical conductivity	$\sigma_{ m thnf}$	$\sigma_{ m hnf}$	$\sigma_{ m nf}$	$\sigma_{ m f}$	$\sigma_{\!_{\! ext{s}1}}$	$\sigma_{\!_{ ext{S2}}}$	$\sigma_{\!_{ m S3}}$
Thermal conductivity	$k_{ m thnf}$	$k_{ m hnf}$	$k_{ m nf}$	$k_{ m f}$	$k_{\rm s1}$	k_{s2}	$k_{\rm s3}$
Nanoparticles' volume fraction					$\widehat{arphi_1}$	$\widehat{\varphi_2}$	\widehat{arphi}_3

$$\frac{\partial f}{\partial t} + u \frac{\partial f}{\partial \xi} + v \frac{\partial f}{\partial \eta} = \left[(1 - \widehat{\varphi}_2) \left[(1 - \widehat{\varphi}_2) \widehat{\varphi}_1 + \widehat{\varphi}_1 \frac{\widehat{P}_{21}}{\widehat{P}_{1}} \right] + \widehat{\varphi}_2 \frac{\widehat{P}_{22}}{\widehat{P}_{1}} \right] + \widehat{\varphi}_3 \frac{\widehat{P}_{22}}{\widehat{P}_{1}} \right]$$

$$\times (1 - \widehat{\varphi}_2)^{2/3} (1 - \widehat{\varphi}_2)^{2/3} (1 - \widehat{\varphi}_2)^{2/3} \frac{1}{Re} \nabla^{i} f$$

$$+ \frac{Mn}{\left[(1 - \widehat{\varphi}_2) \left[(1 - \widehat{\varphi}_1) \widehat{\varphi}_1 + \widehat{\varphi}_1 \frac{\widehat{P}_{21}}{\widehat{P}_{1}} \right] + \widehat{\varphi}_2 \frac{\widehat{P}_{22}}{\widehat{P}_{1}} \right] + \widehat{\varphi}_3 \frac{\widehat{P}_{22}}{\widehat{P}_{1}} \right]} + \frac{\partial \widehat{\theta}}{\widehat{\theta}_3 \frac{\widehat{\theta}_3}{\widehat{\theta}_3}} \right] H \frac{\partial H}{\partial \eta} \frac{\partial \widehat{\theta}}{\partial \xi} - \frac{\partial H}{\partial \xi} \cdot \frac{\partial \widehat{\theta}}{\partial \eta} \right],$$

$$\nabla^2 \widehat{\theta} = \Pr\left\{ \frac{\left[(1 - \widehat{\varphi}_2) \Big[(1 - \widehat{\varphi}_1) \Big] (1 - \widehat{\varphi}_2) \widehat{P}_1 + \widehat{\varphi}_1 \frac{\widehat{P}_{21}}{\widehat{P}_1} \Big] + \widehat{\varphi}_2 \frac{\widehat{P}_{21}}{\widehat{P}_1} \Big] + \widehat{\varphi}_2 \frac{\widehat{P}_{22}}{\widehat{P}_1} \Big] + \widehat{\varphi}_3 \frac{\widehat{P}_{22}}{\widehat{P}_1} \Big] \right\}$$

$$+ \left[(1 - \widehat{\varphi}_3) \Big[(1 - \widehat{\varphi}_1) \Big[(1 - \widehat{\varphi}_2) \widehat{P}_1 + \widehat{\varphi}_1 \frac{\widehat{P}_{22}}{\widehat{P}_1} \Big] + \widehat{\varphi}_2 \frac{\widehat{P}_{22}}{\widehat{P}_1} \Big] + \widehat{\varphi}_3 \frac{\widehat{P}_{22}}{\widehat{P}_1} \Big]$$

$$\times \operatorname{Re}^{*} \left[\frac{(1 - \widehat{\varphi}_2)^2 (1 - \widehat{\varphi}_2)^{2/3} (1 - \widehat{\varphi}_2) \widehat{P}_1 + \widehat{\varphi}_1 \frac{\widehat{P}_{22}}{\widehat{P}_1} \Big] + \widehat{\varphi}_3 \frac{\widehat{P}_{22}}{\widehat{P}_1} \Big] + \widehat{\varphi}_3 \frac{\widehat{P}_{22}}{\widehat{P}_1} \Big]$$

$$+ \operatorname{Pr}^{*} \left[\frac{(1 - \widehat{\varphi}_2)}{(1 - \widehat{\varphi}_1)} \Big[(1 - \widehat{\varphi}_2) \widehat{P}_1 + \widehat{\varphi}_1 \frac{\widehat{P}_{22}}{\widehat{P}_1} \Big] + \widehat{\varphi}_3 \frac{\widehat{P}_{22}}{\widehat{P}_1} \Big] + \widehat{\varphi}_3 \frac{\widehat{P}_{22}}{\widehat{P}_1} \Big]$$

$$\times \operatorname{Re}^{*} \left[\frac{(1 - \widehat{\varphi}_2)}{(1 - \widehat{\varphi}_1)} \Big[(1 - \widehat{\varphi}_2) \widehat{P}_1 + \widehat{\varphi}_1 \frac{\widehat{P}_{22}}{\widehat{P}_1} \Big] + \widehat{\varphi}_3 \frac{\widehat{P}_{22}}{\widehat{P}_1} \Big] + \widehat{\varphi}_3 \frac{\widehat{P}_{22}}{\widehat{P}_1} \Big]$$

$$+ \operatorname{Pr}^{*} \left[\frac{(1 - \widehat{\varphi}_2)}{(1 - \widehat{\varphi}_2)} \Big[(1 - \widehat{\varphi}_2) \widehat{P}_1 + \widehat{\varphi}_1 \frac{\widehat{P}_{22}}{\widehat{P}_1} \Big] + \widehat{\varphi}_3 \frac{\widehat{P}_{22}}{\widehat{P}_1} \Big] + \widehat{\varphi}_3 \frac{\widehat{P}_{22}}{\widehat{P}_1} \Big]$$

$$\times \operatorname{Re}^{*} \left[\frac{(1 - \widehat{\varphi}_2)}{(1 - \widehat{\varphi}_2)} \Big[(1 - \widehat{\varphi}_2) \widehat{P}_1 + \widehat{\varphi}_1 \frac{\widehat{P}_2}{\widehat{P}_1} \Big] + \widehat{\varphi}_3 \frac{\widehat{P}_2}{\widehat{P}_1} \Big] + \widehat{\varphi}_3 \frac{\widehat{P}_2}{\widehat{P}_2} \Big]$$

$$+ \left[(1 - \widehat{\varphi}_2) \Big[(1 - \widehat{\varphi}_2) \Big[(1 - \widehat{\varphi}_2) \widehat{P}_1 + \widehat{\varphi}_1 \frac{\widehat{P}_2}{\widehat{P}_2} \Big] + \widehat{\varphi}_3 \frac{\widehat{P}_2}{\widehat{P}_1} \Big] + \widehat{\varphi}_3 \frac{\widehat{P}_2}{\widehat{P}_2} \Big]$$

$$+ \left[(1 - \widehat{\varphi}_2) \Big[(1 - \widehat{\varphi}_2) \Big[(1 - \widehat{\varphi}_2) \widehat{P}_1 + \widehat{\varphi}_1 \frac{\widehat{P}_2}{\widehat{P}_2} \Big] + \widehat{\varphi}_3 \frac{\widehat{P}_2}{\widehat{P}_2} \Big] + \widehat{\varphi}_3 \frac{\widehat{P}_2}{\widehat{P}_2} \Big] + \widehat{\varphi$$

Table 1: Thermophysical characteristics of THNF and pure nanofluids

Properties	THNF
Density	$\widehat{\rho}_{thnf} = (1 - \widehat{\varphi}_3)[(1 - \widehat{\varphi}_1)\{(1 - \widehat{\varphi}_2)\widehat{\rho}_{f} + \widehat{\varphi}_1\widehat{\rho}_{s1}\} + \widehat{\varphi}_2\widehat{\rho}_{s2}] + \widehat{\varphi}_3\widehat{\rho}_{s3}$
Heat capacity	$(\widehat{\rho} \text{ cp})_{\text{thnf}} = (1 - \widehat{\varphi}_3)[(1 - \widehat{\varphi}_2)\{(1 - \widehat{\varphi}_1)\widehat{\rho}_f + \widehat{\varphi}_1\widehat{\rho}_{s1}\} + \widehat{\varphi}_2\widehat{\rho}_{s2}] + \widehat{\varphi}_3\widehat{\rho}_{s3}$
Viscosity	$\mu_{ m thnf} = \frac{\mu_{ m f}}{(1-\widehat{\varphi}_1)^{2.5}(1-\widehat{\varphi}_2)^{2.5}(1-\widehat{\varphi}_3)^{2.5}}$
Thermal conductivity	$\frac{k_{\text{thnf}}}{k_{\text{hnf}}} = \frac{k_{\text{s3}} + (n-1)(k_{\text{hnf}} - (n-1)\widehat{\varphi}_{\text{s3}})(k_{\text{hnf}} - k_{\text{s3}})}{k_{\text{s3}} + (n-1)k_{\text{hnf}} + \widehat{\varphi}_{\text{s3}}(k_{\text{hnf}} - k_{\text{s3}})},$
	where $\frac{k_{\mathrm{hnf}}}{k_{\mathrm{nf}}} = \frac{k_{\mathrm{S2}} - (n-1)\widehat{\varphi}_2(k_{\mathrm{nf}} - k_{\mathrm{S3}}) + (n-1)k_{\mathrm{nf}}}{k_{\mathrm{S2}} + \widehat{\varphi}_{\mathrm{S2}}(k_{\mathrm{nf}} - k_{\mathrm{S3}}) + (n-1)k_{\mathrm{nf}}}$
	and $\frac{k_{\text{nf}}}{k_{\text{f}}} = \frac{k_{\text{s1}} - (n-1)\widehat{\varphi}_{1}(k_{\text{f}} - k_{\text{s1}}) + (n-1)k_{\text{f}}}{k_{\text{s1}} + \widehat{\varphi}_{1}(k_{\text{f}} - k_{\text{s1}}) + (n-1)k_{\text{f}}}$
Electric conductivity	$\frac{\sigma_{\text{thnf}}}{\sigma_{\text{nf}}} = \frac{\sigma_{83} - 2\widehat{\varphi}_3(\sigma_{\text{nf}} - \sigma_{83}) + 2\sigma_{\text{nf}}}{\sigma_{83} + \widehat{\varphi}_3(\sigma_{\text{nf}} - \sigma_{83}) + 2\sigma_{\text{nf}}},$
	where $\frac{\sigma_{\rm hnf}}{\sigma_{\rm nf}} = \frac{\sigma_{\rm s2} - 2\overline{\varphi}_2(\sigma_{\rm nf} - \sigma_{\rm s2}) + 2\sigma_{\rm nf}}{\sigma_{\rm s2} + \widehat{\varphi}_2(\sigma_{\rm nf} - \sigma_{\rm s2}) + 2\sigma_{\rm nf}}$
	and $\frac{\sigma_{\mathrm{nf}}}{\sigma_{\mathrm{f}}} = \frac{\sigma_{\mathrm{s1}} - 2\widehat{\varphi}_{\mathrm{I}}(\sigma_{\mathrm{f}} - \sigma_{\mathrm{s1}}) + 2\sigma_{\mathrm{f}}}{\sigma_{\mathrm{s1}} + \widehat{\varphi}_{\mathrm{I}}(\sigma_{\mathrm{f}} - \sigma_{\mathrm{s1}}) + 2\sigma_{\mathrm{f}}}$

where

$$H(\xi, \eta) = H_0 \{ \tanh A'_1(\xi - \xi_1) - \tanh A'_2(\xi - \xi_2) \},$$
 (9b)

in the strips defined by $\xi_1 \le \xi \le \xi_2$, $0 \le \eta \le 1$.

The aforementioned equations represent the streamvorticity formulation, which is a modified form of equations (1)–(4) with

$$\widehat{u} = \frac{\partial \widetilde{\psi}}{\partial \eta}, \ \widehat{v} = \frac{\partial \widetilde{\psi}}{\partial \xi} \text{ and } \left[\frac{\partial \widehat{u}}{\partial \eta} - \frac{\partial \widehat{v}}{\partial \xi} \right] = -\widehat{\omega}$$
or
$$\left[\left(\frac{\partial^2 \widetilde{\psi}}{\partial \xi^2} + \frac{\partial^2 \widetilde{\psi}}{\partial \eta^2} \right) \right] = -\widehat{\omega}$$
(10)

In a similar manner, the dimensionless boundary conditions are interpreted as follows:

Left and right walls (Adiabatic)

$$\left(\frac{\partial\theta}{\partial\xi}\right)_{\xi=0} = 0, \left(\frac{\partial\theta}{\partial\xi}\right)_{\xi=1} = 0, \quad \widehat{u}(0, \eta) = \widehat{v}(0, \eta)
= \widehat{u}(1, \eta) = \widehat{v}(1, \eta) = 0, \quad 0 < \eta < 1$$
(11a)

Top wall

$$\widehat{u}(\xi, 1) = 1, \widehat{v}(\xi, 1) = 0, \widehat{\theta}(\xi, 1) = 1, 0 < \xi < 1$$
 (11b)

Bottom wall

$$\widehat{u}(\xi, 0) = 1, \ \widehat{v}(\xi, 0) = 0, \ \widehat{\theta}(\xi, 0) = 1, \ 0 < \xi < 1.$$
 (11c)

Now the Nusselt number and the skin friction are the basic quantities of our interests, which are given by

$$N_u = \frac{\widehat{q} L}{k_{thnf} \Delta T}$$
 and $C_f = \frac{2\tau}{\widehat{\rho}_{thnf} v_0^2}$,

where

$$\widehat{q} = -k_{\rm thnf} \left(\frac{\partial T}{\partial \eta} \right) \left| \begin{array}{c} {\rm Heat} \\ {\rm flux} \end{array} \right. \quad \tau = \widetilde{\mu}_{\rm thnf} \left(\frac{\partial \widehat{U}}{\partial \eta} \right) \left| \begin{array}{c} {\rm Shear} \\ {\rm stress} \end{array} \right.$$

Using the dimensionless variables gives

$$C_{\rm f} {\rm Re} = 2 \frac{(306 \, \widehat{\varphi}^2 - 0.19 \, \widehat{\varphi} + 1)}{\left[1 - \widehat{\varphi} + \widehat{\varphi} \, \frac{\widehat{\rho}_{\rm s}}{\widehat{\rho}_{\rm f}}\right]} \frac{\partial \, \widehat{u}}{\partial y}, \text{ and } {\rm Nu} = \frac{\partial \, \widehat{\theta}}{\partial y}.$$

4 Computational methodology

The combined system of non-dimensional Navier–Stokes, and energy equations (4)–(6) may be numerically solved using an Alternating Direction Implicit (ADI) methodology combined with central difference approximations for the derivatives. A finite difference method is generally the most straightforward numerical technique to perceive and apply when handling differential equations that have structured discretization assumptions. Finite differences can also be helpful in other areas when someone needs to approximate derivatives. In a nutshell, the method is easy to achieve high-order approximations and needs a structured grid.

The details of the scheme in moving from n to (n + 1) time level are given below:

$$\begin{split} \frac{\widehat{w}_{ij}^{(r+1)2} - \widehat{w}_{ij}^{(s)}}{\frac{\partial}{2}} &= \text{Re} \left\{ \frac{(1 - \widehat{\varphi}_{i})^{2} 2^{2} (1 - \widehat{\varphi}_{j})^{2} 2^{2} (1 - \widehat{\varphi}_{j})^{2} 2^{2} (1 - \widehat{\varphi}_{j})^{2} 2^{2}}{\left[(1 - \widehat{\varphi}_{i}) \left[(1 - \widehat{\varphi}_{i}) \right] \left((1 - \widehat{\varphi}_{i}) \widehat{\rho}_{i} + \frac{1}{\widehat{\varphi}_{i}} \frac{\widehat{\alpha}_{i}}{\widehat{\alpha}_{i}} \right] + \widehat{\varphi}_{i} \frac{\widehat{\alpha}_{i}}{\widehat{\beta}_{i}} \right]} \times \underbrace{\left[\widehat{w}_{i-1j}^{(s+1)} - 2\widehat{w}_{ij}^{(s+1)} + \widehat{w}_{i-1j}^{(s+1)} + \widehat{w}_{i-1j}^{(s+1)} \right]}_{K^{2}} \right]}_{+} \underbrace{\left[\widehat{w}_{i-1j}^{(s+1)} - 2\widehat{w}_{ij}^{(s+1)} + \widehat{w}_{i-1j}^{(s)} \right]}_{K^{2}} + \underbrace{\widehat{w}_{i}}_{K^{2}} + \widehat{\varphi}_{i} \frac{\widehat{\beta}_{i}}{\widehat{\beta}_{i}} \right]}_{+} \underbrace{\widehat{w}_{i}}_{K^{2}} + \widehat{\varphi}_{i} \frac{\widehat{\beta}_{i}}{\widehat{\beta}_{i}} \right]}_{+} \underbrace{\widehat{w}_{i}}_{K^{2}} + \widehat{\varphi}_{i}}_{K^{2}} + \widehat{\varphi}_{i} \frac{\widehat{\beta}_{i}}{\widehat{\beta}_{i}} \right]}_{+} \underbrace{\widehat{w}_{i}}_{K^{2}} + \widehat{\varphi}_{i}}_{K^{2}} + \widehat{\varphi}_{i} \frac{\widehat{\beta}_{i}}{\widehat{\beta}_{i}} \right]}_{+} \underbrace{\widehat{w}_{i}}_{K^{2}} + \widehat{\varphi}_{i}}_{+} \underbrace{\widehat{w}_{i}}_{K^{2}} + \widehat{\varphi}_{i}}_{K^{2}} + \widehat{\varphi}_{i}}_{K^{2}}_{K^{2}} + \widehat{\varphi}_{i}}_{K^{2}} + \widehat{\varphi}_{i}}_{K^{2}}_{K^{2}} + \widehat{\varphi}_{i}}_{K^{2}}_{K^{2}}_{K^{2}} + \widehat{\varphi}_{i}}_{K^{2}}_{K^{2}}_{K^{2}} + \widehat{\varphi}_{i}}_{K^{2}}_{K^{2}}_{K^{2}} +$$

$$\frac{\tilde{\psi}_{i-1,j}^{(n+1)} + \tilde{\psi}_{i+1,j}^{(n+1)} - 2\tilde{\psi}_{i,j}^{(n+1)}}{h^2} + \frac{\tilde{\psi}_{i,j-1}^{(n+1)} + \tilde{\psi}_{i,j+1}^{(n+1)} - 2\tilde{\psi}_{i,j}^{(n+1)}}{h^2} = -\widehat{w}_{i,j}^{(n+1/2)},$$
(14)

$$\widehat{u}_{i,j}^{(n+1)} = \frac{-\widetilde{\psi}_{i,j-1}^{(n+1)} + \widetilde{\psi}_{i,j+1}^{(n+1)}}{2k},\tag{15}$$

$$\widehat{\mathbf{v}}_{i,j}^{(n+1)} = -\frac{\widetilde{\psi}_{i+1,j}^{(n+1)} - \widetilde{\psi}_{i-1,j}^{(n+1)}}{2h},\tag{16}$$

$$\begin{split} \frac{\overline{w}_{ij}^{(n+1)} - \overline{w}_{ij}^{(n+\frac{1}{2})}}{\frac{N}{2}} &= \text{Re} \left[\frac{(1 - \overline{\phi}_{i})^{-2i}(1 - \overline{\phi}_{j})^{-2i}(1 - \overline{\phi}_{j})^{-2i}}{\left[(1 - \overline{\phi}_{i})^{2}(1 - \overline{\phi}_{j})^{2} + \overline{w}_{i}^{(n+\frac{1}{2})} + \overline{w}_{i}^{(n+\frac{1}{2})}}{\overline{k}_{i}^{2}} + \overline{w}_{i}^{(n+\frac{1}{2})} + \overline{w}_{i}^{(n+\frac{1}{2})}} \right] \\ &\times \left[\frac{\overline{w}_{i}^{(n+\frac{1}{2})} - 2\overline{w}_{i}^{(n+\frac{1}{2})} + \overline{w}_{i}^{(n+\frac{1}{2})}}{h^{2}} + \overline{w}_{i}^{(n+\frac{1}{2})} + \overline{w}_{i}^{(n+\frac{1}{2})} + \overline{w}_{i}^{(n+\frac{1}{2})}}{h^{2}} \right] \\ &\times \left[\frac{\overline{w}_{i}^{(n+\frac{1}{2})} - 2\overline{w}_{i}^{(n+\frac{1}{2})} + \overline{w}_{i}^{(n+\frac{1}{2})} + \overline{w}_{i}^{(n+\frac{1}{2})}}{h^{2}} + \overline{w}_{i}^{(n+\frac{1}{2})} + \overline{w}_{i}^{(n+\frac{1}{2})} + \overline{w}_{i}^{(n+\frac{1}{2})} + \overline{w}_{i}^{(n+\frac{1}{2})} + \overline{w}_{i}^{(n+\frac{1}{2})}}{h^{2}} \right] \\ &\times H_{ij} \left[\frac{H_{ij+1} - H_{ij+1}}{2h} \frac{\overline{w}_{i+1}^{(n+1)} - \overline{w}_{i+1j}^{(n+1)}}{2h} - \overline{w}_{i+1j}^{(n+1)} - \overline{w}_{i+1j}^{(n+1)} - \overline{w}_{i}^{(n+1)} - \overline{w}_{i}^{(n+1)}}{2h} \right] \\ &\times H_{ij} \left[\frac{W_{ij+1} - H_{ij+1}}{2h} \frac{\overline{w}_{i+1j}^{(n+\frac{1}{2})} - \overline{w}_{i+1j}^{(n+1)} - \overline{w}_{i+1j}^{(n+1)}}{2h} - \overline{w}_{i+1j}^{(n+1)} - \overline{w}_{i}^{(n+1)} - \overline{w}_{i}^{(n+1)}} - \overline{w}_{i+1j}^{(n+1)} - \overline{w}_{i}^{(n+1)} - \overline{w}_{i}^{(n+1)} - \overline{w}_{i}^{(n+1)}}{2h} \right] \\ &\times H_{ij} \left[\frac{\overline{w}_{i+1} - \overline{w}_{i+1j}^{(n+1)}}{2h} + \overline{w}_{i+1j}^{(n+1)} + \overline{w}_{i+1j}^{(n+1)} - \overline{w}_{i}^{(n+1)}} - \overline{w}_{i}^{(n+1)} - \overline{w}_{i}^{(n+1)} - \overline{w}_{i}^{(n+1)} - \overline{w}_{i}^{(n+1)}}{2h} \right] \\ &\times H_{ij} \left[\frac{\overline{w}_{i+1} - \overline{w}_{i+1j}^{(n+1)}}{2h} + \overline{w}_{i+1j}^{(n+1)} + \overline{w}_{i+1j}^{(n+1)} - \overline{w}_{i}^{(n+1)} - \overline{w}_{i}^{(n+1)}} - \overline{w}_{i}^{(n+1)} - \overline{w}_{i}^{(n+1)} - \overline{w}_{i}^{(n+1)}}{2h} \right] \\ &+ \frac{\overline{w}_{i+1} \left[\frac{\overline{w}_{i+1} - \overline{w}_{i+1j}^{(n+1)}}{2h} + \overline{w}_{i}^{(n+1)} + \overline{w}_{i}^{(n+1)} - \overline{w}_{i}^{(n+1)}} - \overline{w}_{i}^{(n+1)} - \overline{w}_{i}^{(n+1)}} - \overline{w}_{i}^{(n+1)} - \overline{w}_{i}^{(n+1)} - \overline{w}_{i}^{(n+1)}}{2h} \right] \\ &+ \frac{\overline{w}_{i+1} \left[\frac{\overline{w}_{i+1} - \overline{w}_{i}^{(n+1)}}{2h} - \overline{w}_{i}^{(n+1)} + \overline{w}_{i}^{(n+1)} - \overline{w}_{i}^{(n+1)} - \overline{w}_{i}^{(n+1)}} - \overline{w}_{i}^{(n+1)} - \overline{w}_{i}^{(n+1)} - \overline{w}_{i}^{(n+1)} - \overline{w}_{i}^{(n+1)}} \right] \\ &+ \frac{\overline{w}_{i+1} - \overline{w}_{i}^$$

The iterative process is finally stopped once the criterion

$$\begin{aligned} & \max\{\text{abs}(\tilde{\psi}_{i,j}^{(n+1)} - \tilde{\psi}_{i,j}^{(n)}), \text{ abs}(w_{i,j}^{(n+1)} - w_{i,j}^{(n)}), \\ & \text{abs}(\theta_{i,j}^{(n+1)} - \theta_{i,j}^{(n)})\} < \text{TOL} \end{aligned}$$

is reached, which identifies that the steady-state solution has arrived. For the purpose of this study, the present problem assumes $TOL < 10^{-6}$. Figure 2 depicts the flow diagram for the pseudo-transient technique.

5 Validation of the numerical technique

In order to confirm the accuracy of our numerical procedure, the numerical results for the horizontal velocity profiles (for the limiting case when $\widehat{\varphi}_1 = \widehat{\varphi}_2 = 0$, Mn = 0, and the flow is driven by only one moving lid), along the three different horizontal lines (y = 0.25, 0.5, 0.75), are compared with ones presented by Yasmin et al. [53] (Figure 3).

To validate the code further, the well-known problem of convection-driven flow in a cavity studied by Chen et al. [55] and Davis [56] is used as a benchmark. The Lattice Boltzmann method and the finite difference method are employed by these studies, respectively.

Table 2 shows that the computational approach used in this study, which yields a Nusselt number that is very consistent with the values reported by the abovementioned

We will explore how governing parameters such as the nanoparticle volume fraction $(0 \le \widehat{\varphi}_1, \widehat{\varphi}_2, \widehat{\varphi}_3 \le 0.20)$, magnetic field localized in the strip $(0.4 \le \xi \le 0.6, \text{ and } 0 \le \eta \le 1)$, Reynolds number $(1 \le \text{Re} \le 200)$, and magnetic number $(0 \le Mn \le 200)$ affect the cavity flow. Water is regarded as the base fluid whereas Ag, Al₂O₃, and TiO₂ (as a mixture) are used as the nanoparticles. Additionally, $\varepsilon = 0$. 02 in our simulations, and the actual properties of water correspond to Pr = 6.2. Due to the comparably lower Reynolds number, it is assumed that the Eckert number is very small. (e.g., 10⁻⁵). Further, the physical properties of the nanoparticles and the base fluid used in the present work can be seen in Table 3.

On other hand, the convergence of our numerical results with the step size may be seen in Figure 4 which not only shows the stability of our numerical scheme but also depicts the independence of the results from the grid size.

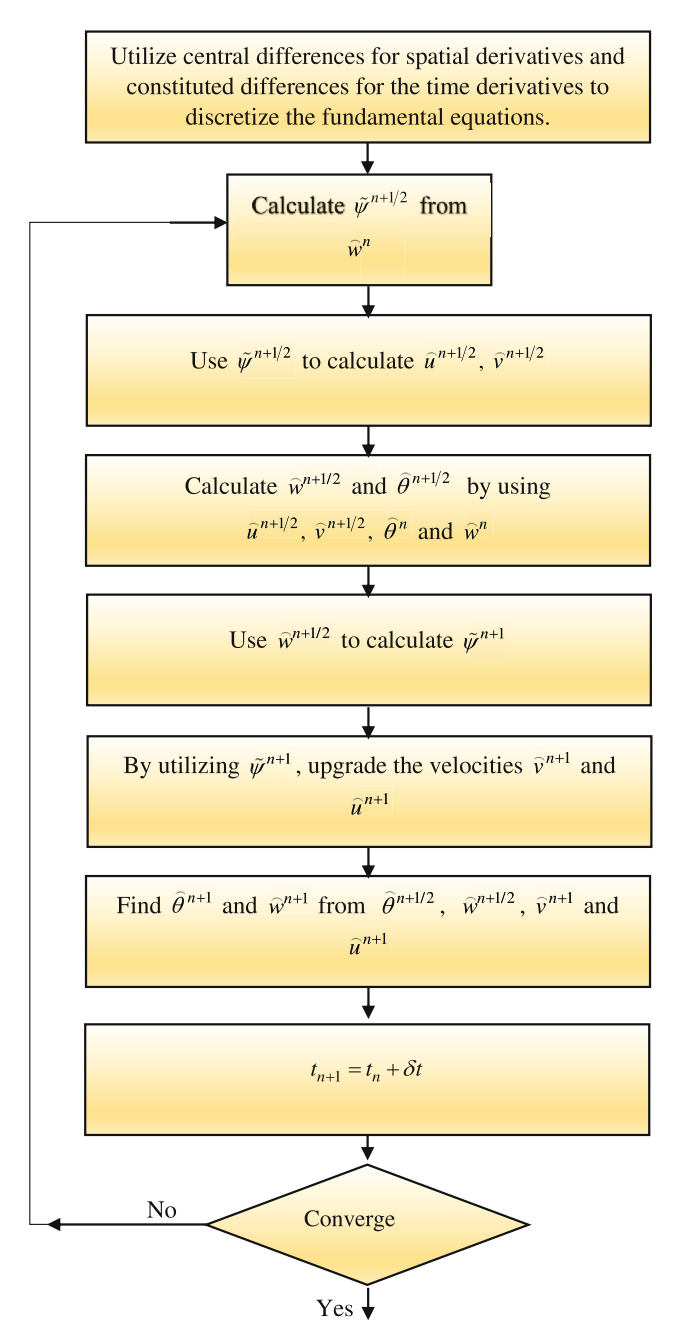


Figure 2: A flow chart of pseudo-transient approach.

6 Results and discussion

This section is devoted to the understanding of results presented in the form of different figures (which include the streamlines, and isotherm) and tables (showing the skin

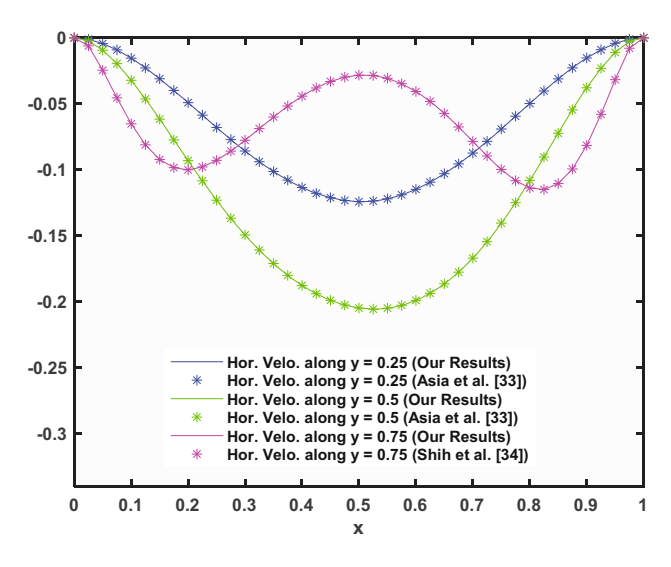


Figure 3: Numerical results in regard with Shih and Tan's analytical solution [54].

Table 2: Comparison of obtained results with literature

Re	Average Nusselt number along the heated wall			
	Lattice Boltzmann method [55]	Finite difference method (Davis [56])	Our approach	
03	1.1192	1.1181	1.1182	
10^{4}	2.2531	2.2432	2.2481	

friction and Nusselt number along the lower and upper horizontal walls of the cavity) for the case when a flow is mainly driven by both horizontal lids of the square cavity moving along the direction of the +ve *x*-axis. Further, the localized magnetic field is also affecting the flow field in the form of a single vertical strip of width 2 units. Finally, the impact of the tri-hybrid nature of the fluid, as well as the intensity of the confined magnetic fields on the Nusselt number and the skin friction factor, will also be discussed.

It is to note that because of having two simultaneous forces, acting in the flow field, such as (i) the inertial force developed by the mechanical effect of the moving lid and (ii) secondly the Lorentz force due to the presence of a

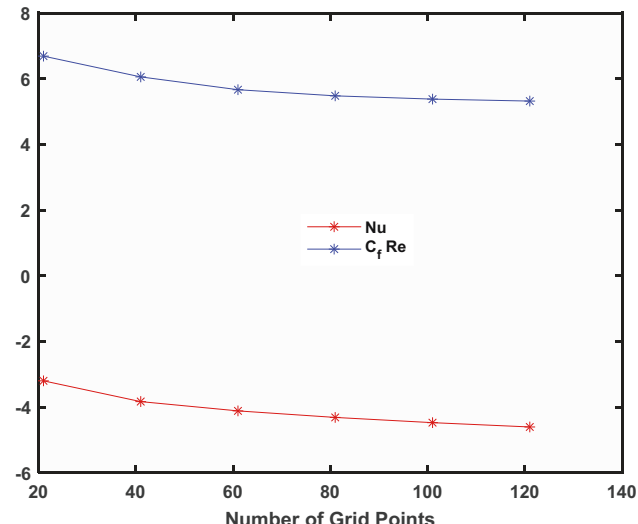


Figure 4: Grid independence analysis.

magnetic source just outside the cavity near the middle of the left vertical wall, the fluid motion becomes more complex and interesting. Further, the low-density fluid generated due to thermal buoyancy force tries to move from heated walls towards the upward direction whereas such movement is opposed by the high-density fluid originating from the strong magnetic force. Our objective, in this section, is to thoroughly investigate how the two forces affect the flow and heat transfer characteristics of the problem.

6.1 Impact of the magnetic parameter

The impact of the intensity of the magnetic field (characterized as a single vertical strip defined in the regions $(0.4 < \xi < 0.6 \text{ and } 0 < \eta < 1)$ on the flow can be seen in Figure 5. In the absence of a magnetic field, two almost symmetric vortices are observed in the flow field. However, the intensity of the magnetic sources elongates the existing vortices which eventually break down to create two new smaller and weaker vortices rotating in clockwise or counter-clockwise directions. It is noted that the direction of the rotation of vortices is determined by the

Table 3: Thermophysical characteristics of water and nanoparticles (Aq-Al₂O₃-TiO₂)

	$C_p(J \text{ kg}^{-1} \text{ K}^{-1})$	βK ⁻¹	$\widehat{ ho}$ (k gm ⁻³)	$\sigma (S \times m^{-1})$	k (W m ⁻¹ K ⁻¹)
Water	4,179	21 × 10 ⁻⁵	997.1	0.05	0.613
Silver (Ag)	235	1.89×10^{-5}	8,933	3.6×10^{7}	429
Aluminum oxide (Al ₂ O ₃)	765	0.85×10^{-5}	3,970	1×10^{-1}	40
Titanium dioxide (TiO ₂)	686	0.90×10^{-5}	5,200	1×10^{-12}	8.95

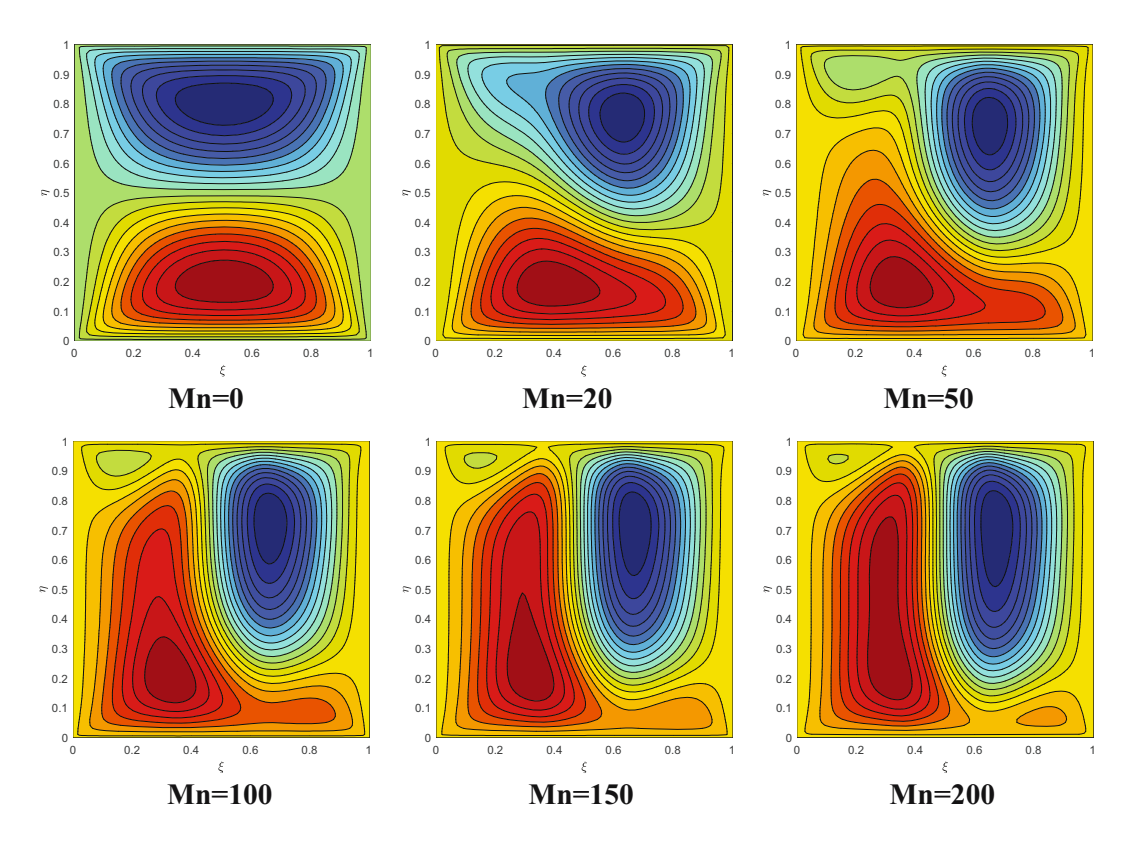


Figure 5: Streamlines representing the flow for various magnetic numbers (Mn).

direction in which the top and bottom lids of the cavity are moving due to some externally imposed mechanical arrangement. In addition, the localized magnetic fields generate a set of counter-rotating vortices (shown in the lighter blue or reddish colors in the streamlines) in the flow which has been created as a result of the break-up of primary vortices. Finally, the elongated vortices in the flow field tend to occupy a major portion of the cavity.

Now, Figure 6 shows how the parameter (Mn) influences the thermal signature across the flow field. In the absence of any magnetic force, it can be seen that the major part of the isotherms is red-colored in the flow field, which predicts a relatively higher temperature. Further, a concentration of isotherms is also noted near the top wall of the cavity. The magnetic force, on the other hand, eliminates any linear temperature distribution in any part of the cavity. Additionally, it is possible to detect a decrease in the thermal gradient near the lower horizontal wall of the enclosure.

6.2 Impact of the Reynolds number

The effect of the Reynolds number on the flow may be seen in Figure 7. It is to note that if the dimension of the cavity

and the properties of the fluid are constant, an increase in the Reynolds number would simply mean an enhancement in the velocity with which the lids are moving. So, in this way, the Reynolds number may be connected with the lid velocity. At smaller Re, an increase in the parameter results in the elongation of two primary vortices, thus giving rise to new vortices occupying the flow field.

The effect of the Reynolds number on the thermal distribution can be seen in Figure 8. As discussed earlier, an increase in the Reynolds number translates into a rise in the velocity of the moving lids, subject to the condition that the fluid properties and the size of the cavity are fined. The faster moving lids will cause a more rigorous mixing of the layer of fluid at different temperatures. This will obviously distort any uniformity in the pattern of the isotherms. Finally, similar to the magnetic parameter, a concentration of isotherms near the upper horizontal wall of the enclosure has been identified.

6.3 Impact of localization

An obvious point to ponder may be the role of the width of the magnetic field in the present problem. To understand

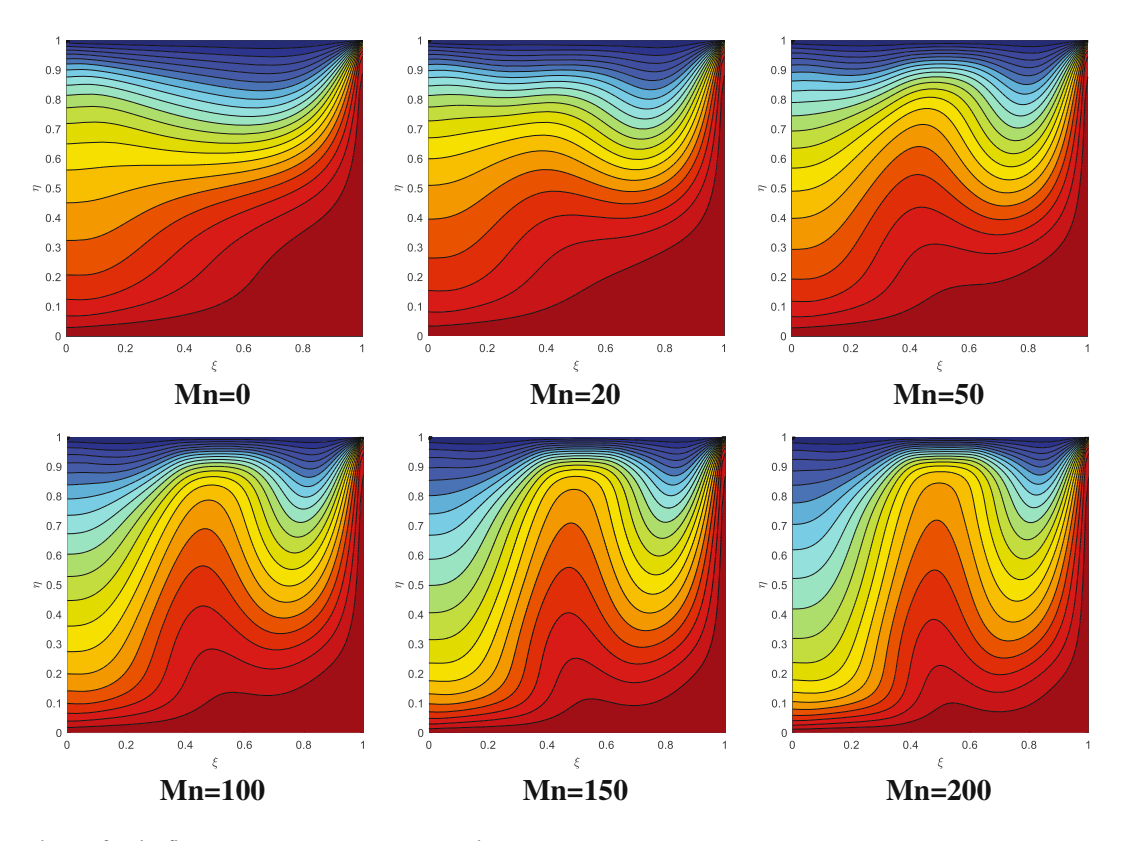


Figure 6: Isotherms for the flow against various magnetic numbers (Mn).

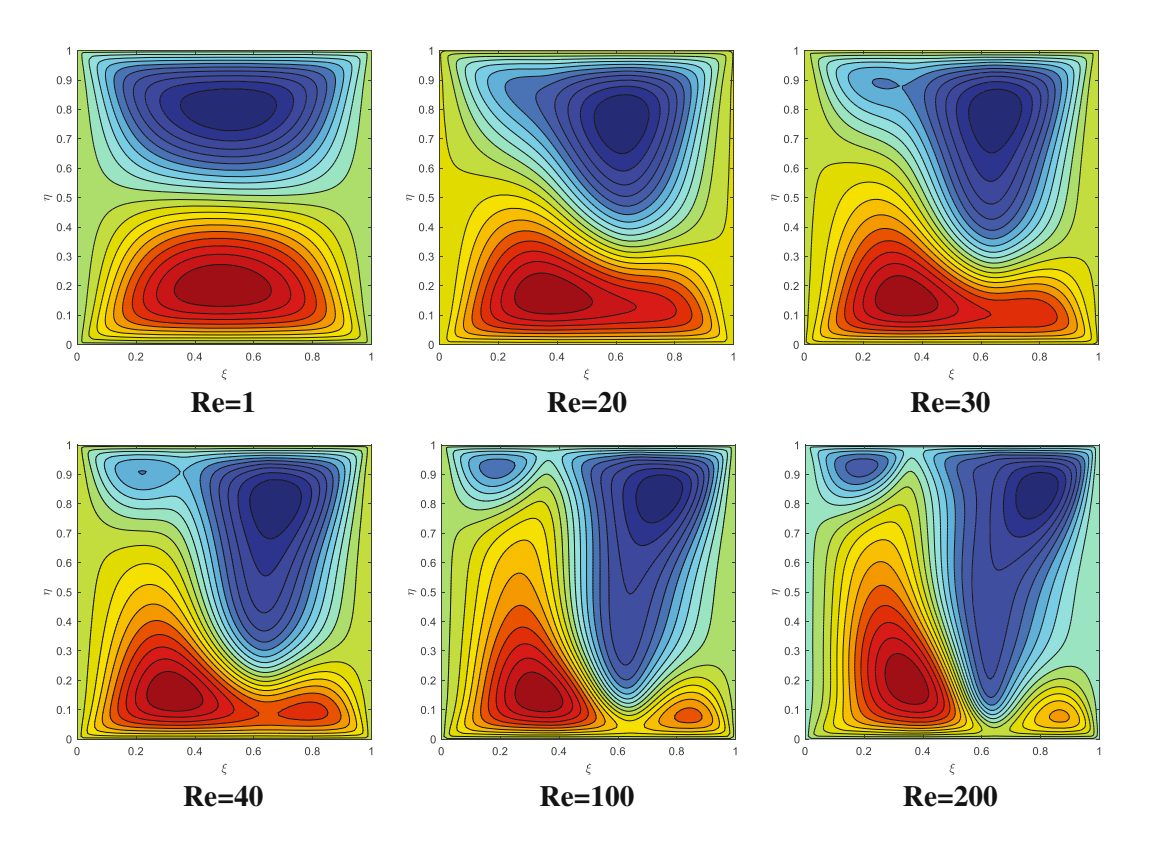


Figure 7: Streamlines representing the flow for various Reynolds numbers (Re).

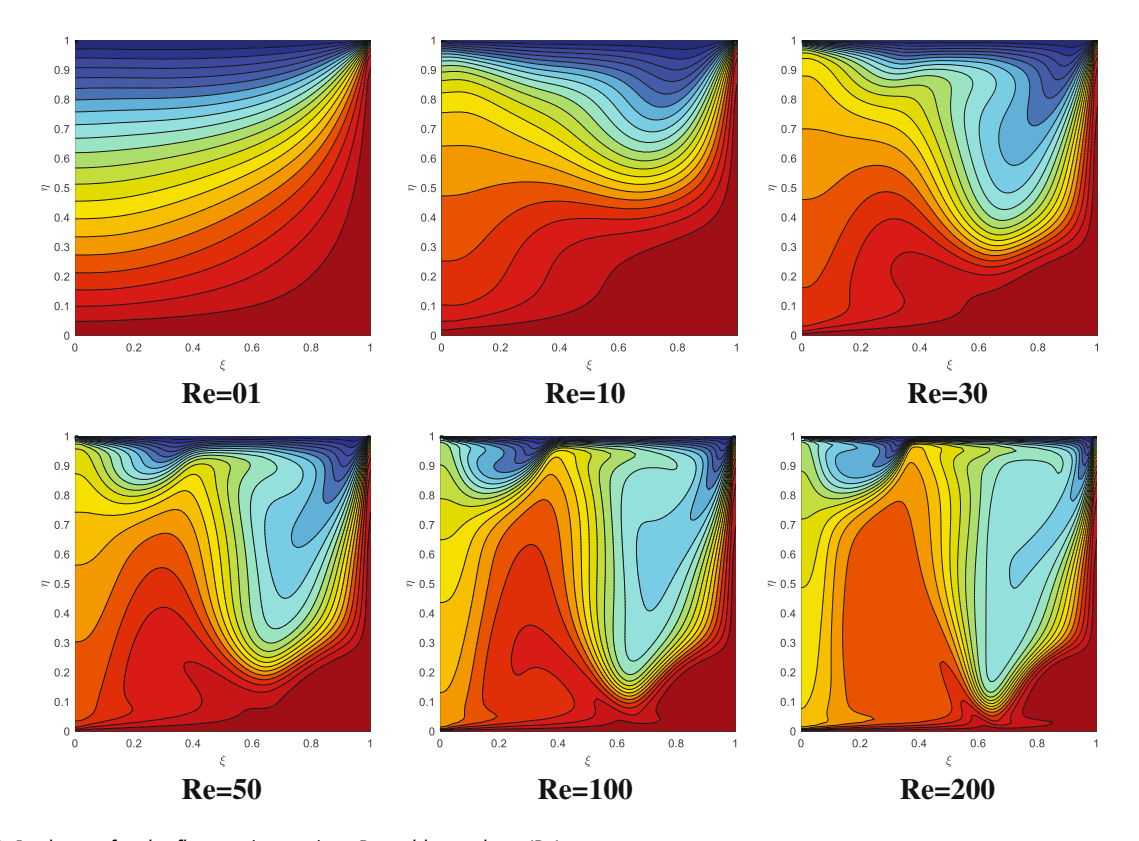


Figure 8: Isotherms for the flow against various Reynolds numbers (Re).

this, a single strip defined by $(0.4 - L) < \xi < (0.6 + L)$, and $0 < \eta < 1$), within the flow field has been considered. It is clear from Figure 9 that the parameter L determines the width of the strip, obviously, L = 0.4, corresponds to the case when the magnetic field is occupying the whole cavity whereas L = 0.0 is the case when the magnetic field is confined to the strip $(0.4 < \xi < 0.6$, and $0 < \eta < 1$). It is to point out that the confinement of the magnetic field intensity gives rise to new vortices while elongating the primary vortices. The isotherms, on the other hand, are squeezed towards the upper horizontal lid thus giving rise to higher temperature gradients in this region (Figure 10).

6.4 Nusselt number and skin friction dependence on different parameters

Let us now go over how the Nusselt number (Nu) and the skin friction factor (C_f Re) vary with the governing parameter Mn and Re for the same range of two parameters. The Nu and C_f Re profiles as shown in Figures 11 and 12 are drawn. It is clear that the magnetic parameter significantly enhances heat transfer. On the other hand, the Reynolds number causes a significant rise in the Nusselt number.

However, this rise is much more in magnitude than for the magnetic number (for the same range of the two parameters). Finally, as for the skin friction factor CfRe is concerned, it shows that the two parameters influence the CfRe in the same qualitative sense. The quantitative impact may, however, be a little bit different as expected, the particle volume fraction φ_1 , φ_2 and φ_3 cause a notable rise in the Nusselt number with a comparatively lower impact on the skin friction (CfRe). However, compared to φ_2 and φ_3 , the Nusselt number depends more strongly on φ_1 due to the inherent physical properties of the nanoparticles. It has also been noted that the localization or confinement of the magnetic field does not always increase or decrease the Nusselt number. Thus, it is concluded that there will be a certain width of the magnetic corridor for which the Nusselt number would be optimal. However, this may be the topic of a subsequent study.

6.5 Impact of the solid volume-fraction (Ag, Al₂O₃, and TiO₂)

The following analysis focuses on how a magnetic field, Reynolds Number, the nanoparticle volume fractions, Nusselt number, and skin friction interact with each

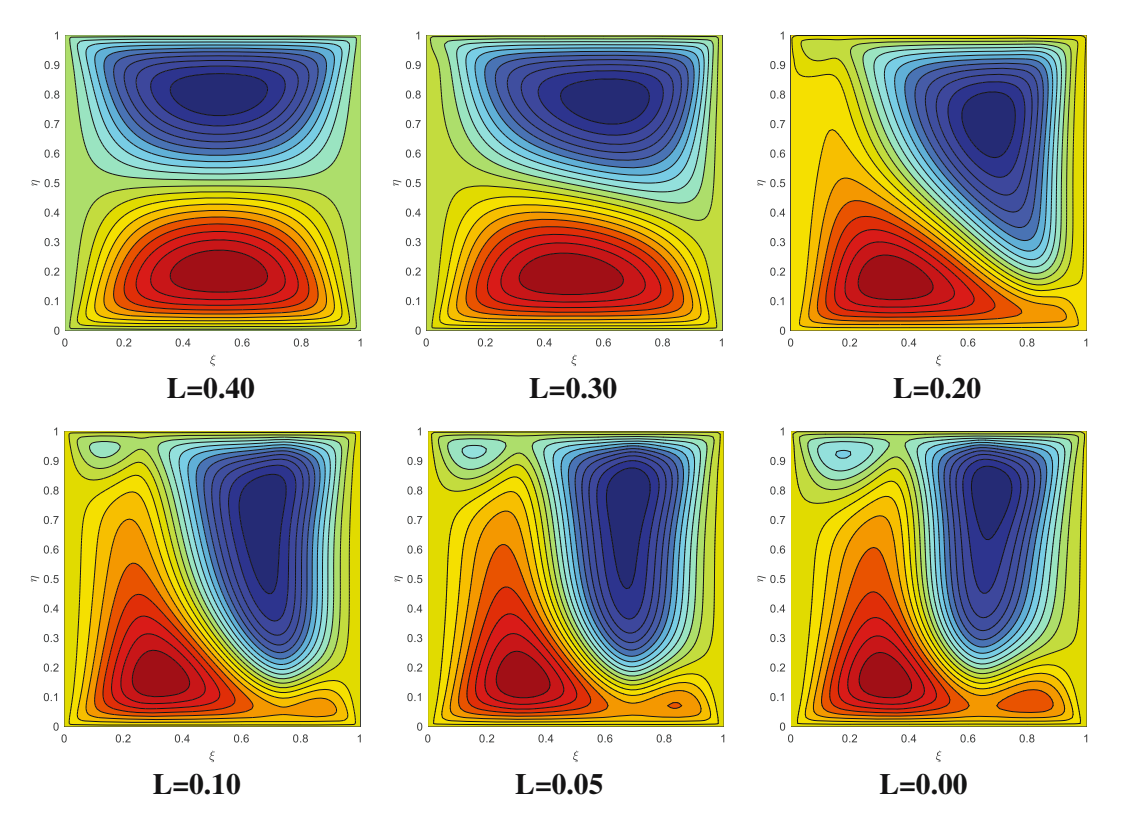


Figure 9: Streamlines for various values of the magnetic strip length (l).

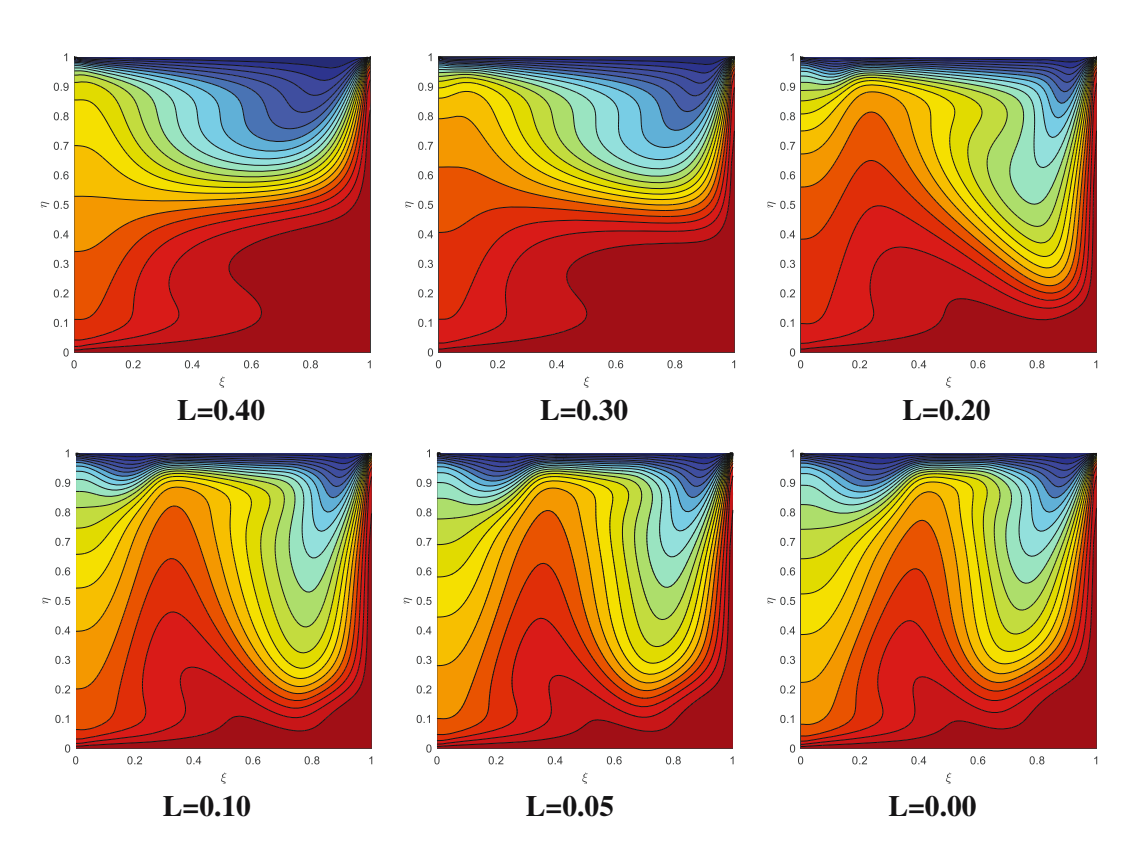


Figure 10: Isotherms for various values of the magnetic strip length (*L*).

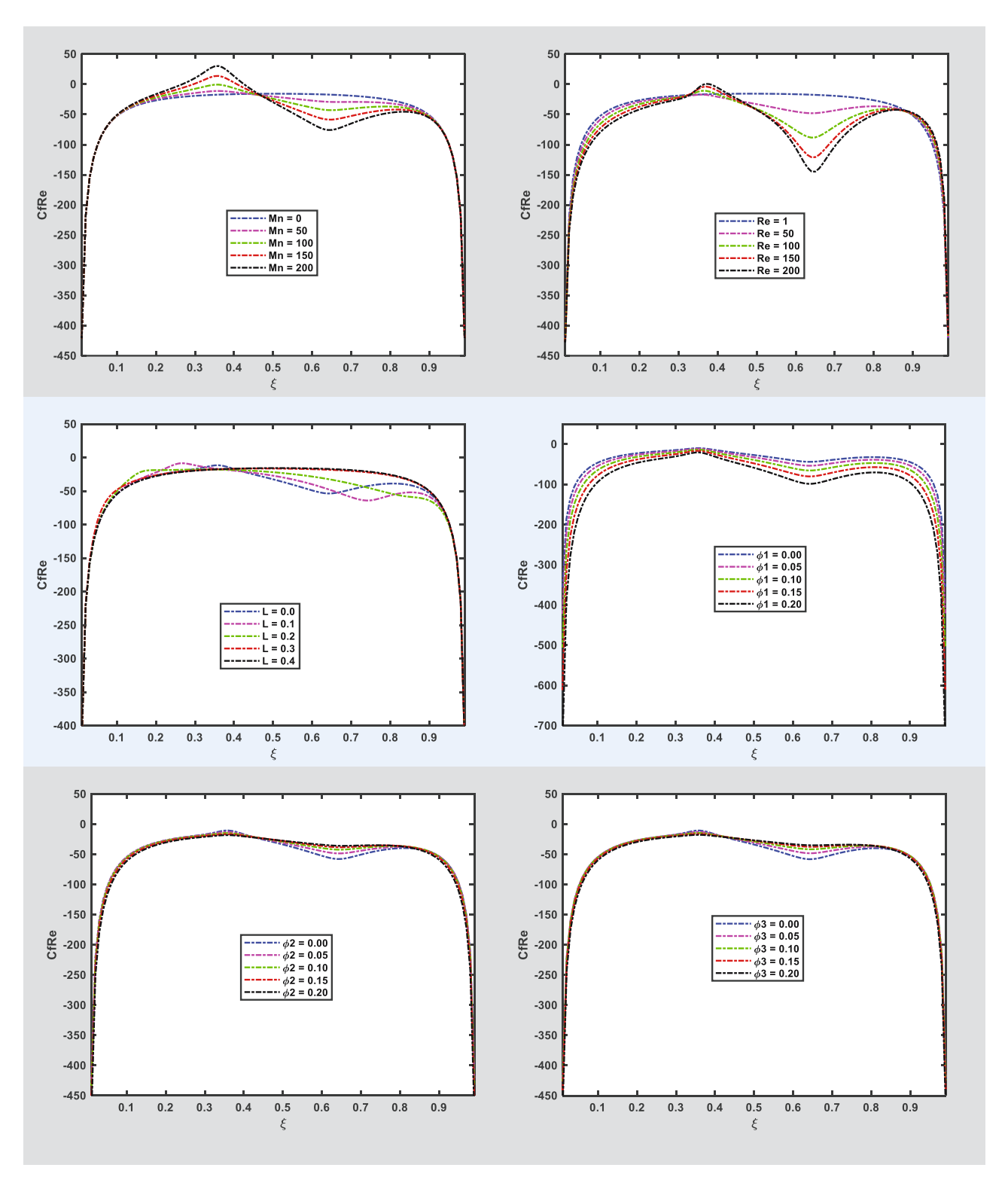


Figure 11: Dependence of skin friction on different parameters.

18 — Shabbir Ahmad *et al.*

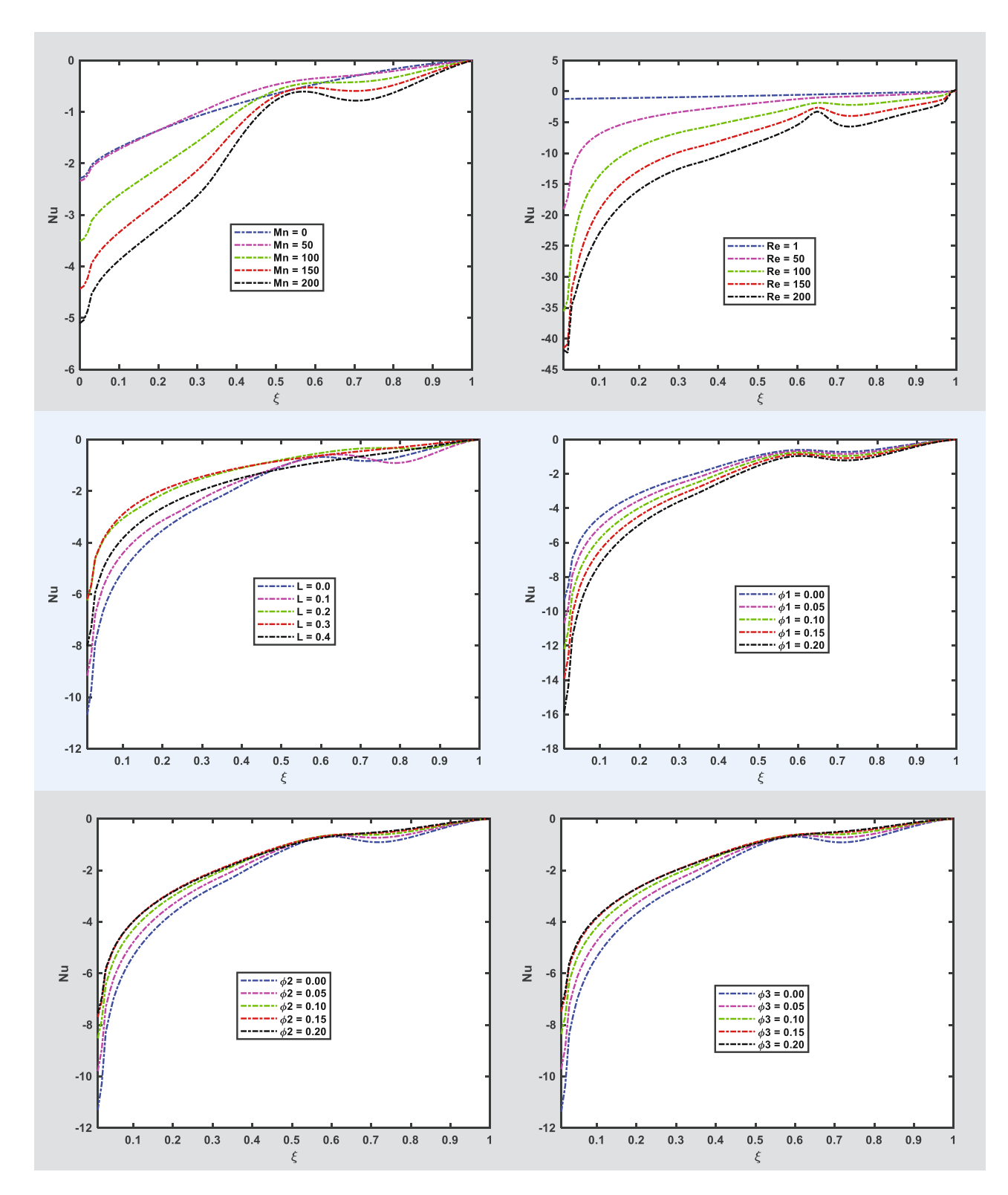


Figure 12: Dependence of Nusselt number on different parameters.

other. Unless otherwise stated, we have fixed Mn = 5, Re = 5, $\widehat{\varphi}_1$ = 0.05, $\widehat{\varphi}_2$ = 0.02, and $\widehat{\varphi}_3$ = 0.02. Table 4 shows that the magnetic field intensity may result in up to 13 and 119% increase in the skin friction and Nusselt number, respectively. On the other hand, a remarkable change in the Nusselt number and the skin friction is also observed by raising the Reynolds number Re (Table 5).

It is evident from Tables 6–8 that the Nusselt number (Nu) increased by 62% for $\widehat{\varphi}_1$, while decreased by almost 25% for $\widehat{\varphi}_2$ and $\widehat{\varphi}_3$. Moreover, there is a significant decrease (113%) in skin friction for $\widehat{\varphi}_1$, while, on the other hand, there is a similar amount of (but reverse) change for $\widehat{\varphi}_2$ and $\widehat{\varphi}_3$. This means that $\widehat{\varphi}_1$ is more impactful on skin friction in comparison to $\widehat{\varphi}_2$ and $\widehat{\varphi}_3$ when there is 20% rise for nanostructures in the base fluid.

With the understanding that the parameter L actually determines one of the geometric dimensions of the rectangle in which the magnetic field is localized, it can be concluded (from Table 9) that the occupation of the magnetic field in a wider part of the domain results in a serious decline in both the Nusselt number and the skin friction factor.

6.6 Comparison of thermal performance of the nanoparticles

There are two things that may be inferred from Figure 13: one there is almost a linear relationship between the average Nusselt number (along the vertical wall adjacent

Table 4: Variation in Nu and \mathcal{C}_f with Mn

Mn	Nu	$ C_{\mathrm{f}}\mathrm{Re} $
00	0.7699	46.7320
50	0.7319	48.8759
100	1.0854	50.4625
150	1.4127	51.7376
200	1.6864	52.8780

Table 5: Variation in Nu and C_f with Re

Re	Nu	$ \mathcal{C}_{\mathrm{f}}\mathrm{Re} $
01	0.6724	46.6926
50	3.0374	56.1526
100	6.1516	64.0634
150	8.7981	69.1599
200	10.8247	73.0435

Table 6: Variation in Nu and C_f with $(\widehat{\varphi}_1)$ for Re = 20 and Mn = 20

\widehat{arphi}_1	Nu	C _f Re
0.00	1.8494	46.8612
0.05	2.1034	55.9203
0.10	2.3784	67.2506
0.15	2.6792	81.5945
0.20	3.0115	99.9932

Table 7: Variation in Nu and $C_{\rm f}$ with $(\widehat{\varphi}_2)$

\widehat{arphi}_2	Nu	$ C_{\rm f}{ m Re} $
0.00	2.2016	56.8119
0.05	1.9618	55.0545
0.10	1.7590	54.7303
0.15	1.6392	55.6909
0.20	1.6473	57.9029

Table 8: Variation in Nu and C_f with $(\widehat{\varphi}_3)$

\widehat{arphi}_3	Nu	$ C_{\mathrm{f}}\mathrm{Re} $
0.00	2.2153	57.1067
0.05	1.9449	54.6858
0.10	1.7212	53.8729
0.15	1.5858	54.4275
0.20	1.5780	56.2618

Table 9: Variation in Nu and $C_{\rm f}$ with L

L	Nu	$c_{ m f}$
00	2.1034	55.9203
0.10	1.9053	57.0784
0.20	1.2740	53.4481
0.30	1.2361	46.2474
0.35	1.6694	46.7971

to the magnetic source) and the nanoparticle volume fraction, second, the THNF containing Ag, Al_2O_3 , and TiO_2 outperforms in terms of enhancing the average Nusselt number, compared to the simple nanofluid with Ag, Al_2O_3 , or TiO_2 particles.

6.7 Impact of magnetic field intensity

It is to point that ξ_1 , ξ_2 , ξ_3 , and ξ_4 appearing in equation (9b) define the two magnetic fields, confined in the form of two

vertical strips, as $\xi_1 \le \xi \le \xi_2$, $\xi_3 \le \xi \le \xi_4$ and $0 \le \eta \le 1$. Further, the parameter A_1 and A_2 determine the amplitude of the magnetic field. Now the impact of the parameter A_1 and A_2 on the average Nusselt number is shown in Figure 14. It is obvious that the Nusselt number depends more on A_1 and A_2 at their smaller values.

6.8 Impact of the localization of magnetic field

The magnetic strip is defined as follows: $0.4 - L \le x \le 0.6 + L$, $0 \le \eta \le 1$. This means that the case L = 0 indicates that the strip has a fixed width of 0.2 units. As L is increased (that is, when the strip is widened), it is noted that the Nusselt number first decreases and then increases. Further, the Nusselt number is more sensitive to the nanoparticle concentration at the larger value of $\widehat{\varphi}_1$, $\widehat{\varphi}_2$, and $\widehat{\varphi}_3$ (Figure 15).

7 Concluding remarks

The novelty or originality of the study lies in the combination of lid-driven cavity flow, localized magnetic field, and THNFs, which introduce additional boundary conditions. Most of the scientific literature is enriched with investigations dealing with problems assuming a uniform magnetic field occupying the flow field. But in this investigation, a vertical strip of magnetism within the flow field has been introduced. It may be the first effort to interpret the role of the applied magnetic field in the formation of the new

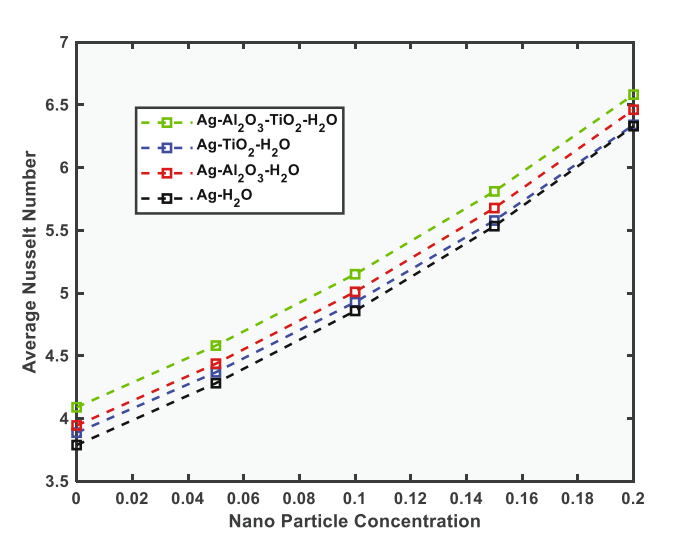


Figure 13: Comparison of concerned nanoparticles with THNF.

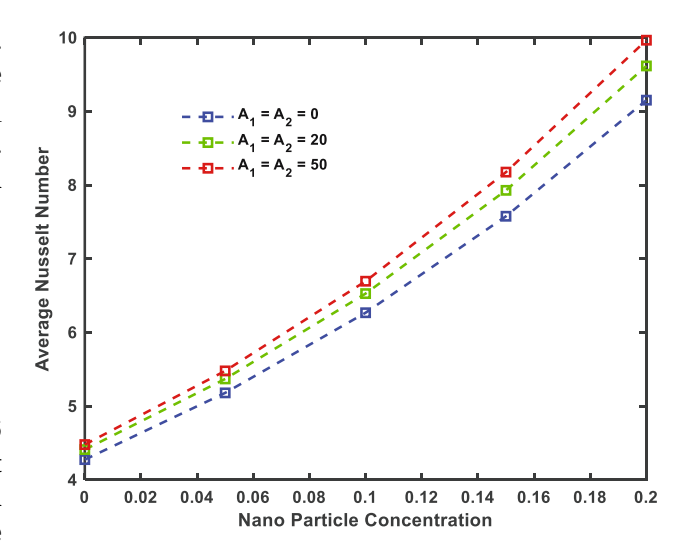


Figure 14: Impact of the parameter A_1 and A_2 on average Nusselt number.

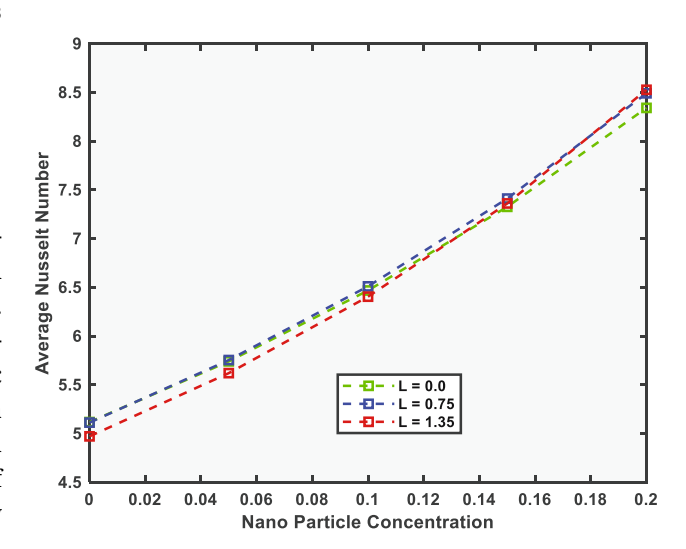


Figure 15: Impact of the magnetic strip width on the average Nusselt number.

vortices in the flow field. The following conclusions may be drawn.

Without any magnetic field, the flow field shows a couple of primary vortices. But when the magnetic sources are turned on, they stretched and tore apart the vortices, creating two new weaker ones that spin in opposite directions. The magnetic fields have a significant impact on the flow field, as it breaks up the primary vortices into a collection of counter-rotating vortices. This results in a complex pattern of many vortices that have different sizes and shapes. One notable feature of this pattern is that the elongated vortices tend to occupy a large portion of the cavity, making them more visible and dominant than the others. The isotherms have a relatively higher

temperature without the magnetic force. The magnetic field also makes the isotherms more concentrated near the upper wall of the enclosure, where the temperature gradient is higher. The magnetic force also affects the temperature distribution in the enclosure, as it disrupts the uniform temperature distribution in the cavity, creating a more varied pattern. It also lowers the temperature difference near the bottom wall of the cavity, making it less hot than before. When the fluid properties and cavity size are carefully tuned, the velocity of the moving lids increases with the Reynolds number. The faster moving lids mixed the fluid layers at different temperatures, disrupting the uniform pattern of the isotherms. Moreover, like a magnetic parameter, the isotherms clustering near the upper horizontal wall of the enclosure have also been observed. The primary vortices stretch and split into new ones when the magnetic field intensity is confined. Meanwhile, the isotherms squeeze towards the top horizontal lid, creating higher temperature gradients in that area. The magnetic field and Reynolds number affect the skin friction factor in the same way, but not by the same amount. The particle volume fraction boosts the Nusselt number more than the skin fraction. The Nusselt number also depends more on aluminum oxide, because of its physical properties. The Nusselt number can go up or down depending on how the magnetic field is confined or localized. This means that there is an optimal magnetic corridor width for the Nusselt number. The magnetic field intensity has a strong influence on the Nusselt number and skin friction, as it can make them increase by up to 119 and 13%, respectively. Similarly, the Reynolds number also has a remarkable impact on the Nusselt number and skin friction, as it changes the velocity of the moving lids. The average Nusselt number increases almost linearly with the nanoparticle volume fraction. Moreover, the THNF with Ag, Al₂O₃, and TiO₂ boosts the average Nusselt number more than the conventional nanofluids such as Ag, Al₂O₃, or TiO₂. The Nusselt number drops first and then rises. It is more sensitive to the high nanoparticle concentration, as it affects the heat transfer rate.

An interesting future direction emerging from the current study may be the consideration of multiple magnetic sources producing fields of different intensities within the flow regime in the form of localized strips, which may result in multiple vortices of different strengths.

Acknowledgments: The authors extend their appreciation to King Saud University for funding this work through Researchers Supporting Project number (RSPD2023R711), King Saud University, Riyadh, Saudi Arabia.

Funding information: The Researchers Supporting Project number (RSPD2023R711), King Saud University, Riyadh, Saudi Arabia.

Author contributions: All authors have accepted responsibility for the entire content of this manuscript and approved its submission.

Conflict of interest: The authors state no conflict of interest.

Data availability statement: The datasets generated during and/or analyzed during the current study are available from the corresponding author on reasonable request.

References

- Abdullah N, Ismail Z, Halifi AS, Che Ayob AR, Kasiman EH, Saidina [1] Amin N. Numerical computations of biomagnetic fluid flow in a lid driven cavity. CFD Lett. 2020;12(4):43-53.
- Hajesfandiari A, Dargush GF, Hadjesfandiari AR. Size-dependent fluid dynamics with application to lid-driven cavity flow. J Non-Newtonian Fluid Mech. 2015;223:98-115.
- [3] Biswas S, Kalita JC. Topology of corner vortices in the lid-driven cavity flow: 2D vis a vis 3D. Arch Appl Mech. 2020;90:2201-16.
- Ouyang G, Abed-Meraim K. A Survey of Magnetic-Field-Based Indoor Localization. Electronics. 2022;11(6):864.
- Siebler B, Sand S, Hanebeck UD. Localization with magnetic field [5] distortions and simultaneous magnetometer calibration. IEEE Sens I. 2020:21(3):3388-97.
- Jalili P, Narimisa H, Jalili B, Ganji DD. Micro-polar nanofluid in the presence of thermophoresis. Hall current, and Brownian motion in a rotating system. Mod Phys Lett B. 2023;37:2250197.
- Abdel-Nour Z, Aissa A, Mebarek-Oudina F, Rashad AM, Ali HM, Sahnoun M, et al. Magnetohydrodynamic natural convection of hybrid nanofluid in a porous enclosure: numerical analysis of the entropy generation. J Therm Anal Calorim. 2020;141:1981-92.
- Armaghani T, Sadeghi MS, Rashad AM, Mansour MA, Chamkha AJ, Dogonchi AS, et al. MHD mixed convection of localized heat source/ sink in an Al₂O₃-Cu/water hybrid nanofluid in L-shaped cavity. Alex Eng J. 2021;60(3):2947-62.
- Dinarvand S, Berrehal H, Tamim H, Sowmya G, Noeiaghdam S, Abdollahzadeh M. Squeezing flow of aqueous CNTs-Fe₃O₄ hybrid nanofluid through mass-based approach: Effect of heat source/ sink, nanoparticle shape, and an oblique magnetic field. Results Eng. 2023;17:100976.
- [10] Rahimi A, Kasaeipoor A, Amiri A, Doranehgard MH, Malekshah EH, Kolsi L. Lattice Boltzmann method based on Dual-MRT model for three-dimensional natural convection and entropy generation in CuO-water nanofluid filled cuboid enclosure included with discrete active walls. Comput Math Appl. 2018;75(5):1795-813.
- Salari M, Malekshah EH, Malekshah MH. Hydrothermal analysis of transient natural convection in a finned cavity filled with sulfuric acid-water (25-75%) for applications in high-performance lead-acid batteries-Numerical study. Therm Sci Eng Prog. 2017;4:241-51.

- [12] Salari M, Rashidi MM, Hasani ME, Hasani MM. Numerical analysis of turbulent/transitional natural convection in trapezoidal enclosures. Int J Numer Methods Heat Fluid Flow. 2017;27(12):2902–23.
- [13] Gorla RSR, Siddiqa S, Mansour MA, Rashad AM, Salah T. Heat source/sink effects on a hybrid nanofluid-filled porous cavity. J Thermophys Heat Transf. 2017;31(4):847–57.
- [14] Rashad AM, Chamkha AJ, Ismael MA, Salah T. Magnetohydrodynamics natural convection in a triangular cavity filled with a Cu-Al₂O₃/ water hybrid nanofluid with localized heating from below and internal heat generation. J Heat Transf. 2018;140(7):072502.
- [15] Ali K, Ahmad S, Ahmad S, Ashraf M, Asif M. On the interaction between the external magnetic field and nanofluid inside a vertical square duct. AIP Adv. 2015;5(10):107120.
- [16] Basri EI, Sultan M, Basri AA, Mustapha F, Ahmad KA. Numerical study of Lorentz force interaction with micro structure in channel flow. Energies. 2021;14(14):4286.
- [17] Ahmad S, Cai J, Ali K. Prediction of new vortices in single-phase nanofluid due to dipole interaction. J Therm Anal Calorim. 2020:140:1–15.
- [18] Ali K, Ahmad S, Ahmad S, Jamshed W, Hussain SM, Tag El Din ESM. Molecular interaction and magnetic dipole effects on fully developed nanofluid flowing via a vertical duct applying finite volume methodology. Symmetry. 2022;14(10):2007.
- [19] Kai Y, Ahmad S, Takana H, Ali K, Jamshed W, Eid MR, et al. Thermal case study and generated vortices by dipole magnetic field in hybridized nanofluid flowing: Alternating direction implicit solution. Results Phys. 2023;49:106464.
- [20] Ali K, Ahmad S, Ahmad S, Tayebi T. Impact of magnetic field localization on the vortex generation in hybrid nanofluid flow. J Therm Anal Calorim. 2023;148:6283–300.
- [21] Kai Y, Ali K, Ahmad S, Ahmad S, Jamshed W, Raizah Z, et al. A case study of different magnetic strength fields and thermal energy effects in vortex generation of ${\rm Ag\text{-}TiO_2}$ hybrid nanofluid flow. Case Stud Therm Eng. 2023;47:103115.
- [22] Ayub R, Ahmad S, Ahmad S, Akhtar Y, Alam MM, Mahmoud O. Numerical assessment of dipole interaction with the single-phase nanofluid flow in an enclosure: A pseudo-transient approach. Materials. 2022;15(8):2761.
- [23] Liu C, Farouk N, Ayed H, Aouaini F, Bouzgarrou SM, Mouldi A, et al. Simulation of MHD free convection inside a square enclosure filled porous foam. Case Stud Therm Eng. 2022;32:101901.
- [24] Roy NC. MHD natural convection of a hybrid nanofluid in an enclosure with multiple heat sources. Alex Eng J. 2022;61(2):1679–94.
- [25] Algehyne EA, Alrihieli HF, Bilal M, Saeed A, Weera W. Numerical approach toward ternary hybrid nanofluid flow using variable diffusion and non-Fourier's concept. ACS Omega. 2022;7(33):29380–90.
- [26] Adun H, Kavaz D, Dagbasi M. Review of ternary hybrid nanofluid: Synthesis, stability, thermophysical properties, heat transfer applications, and environmental effects. J Clean Prod. 2021;328:129525.
- [27] Shah TR, Koten H, Ali HM. Chapter 5 Performance effecting parameters of hybrid nanofluids. In: Ali HM, editor. Hybrid nanofluids for convection heat transfer. Academic Press; 2020. p. 179–213. doi: 10.1016/B978-0-12-819280-1.00005-7.
- [28] Jakeer S, BalaAnki Reddy P, Rashad AM, Nabwey HA. Impact of heated obstacle position on magneto-hybrid nanofluid flow in a liddriven porous cavity with Cattaneo-Christov heat flux pattern. Alex Eng J. 2021;60(1):821–35.

- [29] Jalili P, Sadeghi Ghahare A, Jalili B, Domiri Ganji D. Analytical and numerical investigation of thermal distribution for hybrid nanofluid through an oblique artery with mild stenosis. SN Appl Sci. 2023;5(4):95.
- [30] Abdollahi SA, Jalili P, Jalili B, Nourozpour H, Safari Y, Pasha P, et al. Computer simulation of Cu: AlOOH/water in a microchannel heat sink using a porous media technique and solved by numerical analysis AGM and FEM. Theor Appl Mech Lett. 2023;13:100432.
- [31] Tawade JV, Guled CN, Noeiaghdam S, Fernandez-Gamiz U, Govindan V, Balamuralitharan S. Effects of thermophoresis and Brownian motion for thermal and chemically reacting Casson nanofluid flow over a linearly stretching sheet. Results Eng. 2022;15:100448.
- [32] Skoryna J, Wachowiak M, Marczyńska A, Rogowska A, Majchrzycki Ł, Koczorowski W, et al. Correlation between interlayer exchange coupling and hydrogen absorption in V-Fe layered structures. Surf Coat Technol. 2016;303:119–24.
- [33] Skoryna J, Marczyńska A, Smardz L. XPS studies of nanocrystalline La–Ni and LaNi_{5- x}Alx (x = 0.2, 0.5, 1) alloy thin films. J Alloy Compd. 2015;645:S384–7.
- [34] Hameed N, Noeiaghdam S, Khan W, Pimpunchat B, Fernandez-Gamiz U, Khan MS, et al. Analytical analysis of the magnetic field, heat generation and absorption, viscous dissipation on couple stress casson hybrid nano fluid over a nonlinear stretching surface. Results Eng. 2022;16:100601.
- [35] Xiong Q, Altnji S, Tayebi T, Izadi M, Hajjar A, Sundén B, et al. A comprehensive review on the application of hybrid nanofluids in solar energy collectors. Sustain Energy Technol Assess. 2021;47:101341.
- [36] Rahimi A, Sepehr M, Lariche MJ, Mesbah M, Kasaeipoor A, Malekshah EH. Analysis of natural convection in nanofluid-filled Hshaped cavity by entropy generation and heatline visualization using lattice Boltzmann method. Phys E: Low-Dimens Syst Nanostruct. 2018;97:347–62.
- [37] Ho CJ, Liu WK, Chang YS, Lin CC. Natural convection heat transfer of alumina-water nanofluid in vertical square enclosures: An experimental study. Int J Therm Sci. 2010;49(8):1345–53.
- [38] Turcu R, Darabont AL, Nan A, Aldea N, Macovei D, Bica D, et al. New polypyrrole-multiwall carbon nanotubes hybrid materials. J Optoelectron Adv Mater. 2006;8(2):643–7.
- [39] Jalili P, Narimisa H, Jalili B, Shateri A, Ganji DD. A novel analytical approach to micro-polar nanofluid thermal analysis in the presence of thermophoresis, Brownian motion and Hall currents. Soft Comput. 2023;27(2):677–89.
- [40] Mansour MA, Siddiqa S, Gorla RSR, Rashad AM. Effects of heat source and sink on entropy generation and MHD natural convection of Al₂O₃-Cu/water hybrid nanofluid filled with square porous cavity. Therm Sci Eng Prog. 2018;6:57–71.
- [41] Jalili P, Ahmadi Azar A, Jalili B, Asadi Z, Domiri Ganji D. Heat transfer analysis in cylindrical polar system with magnetic field: A novel Hybrid Analytical and Numerical Technique. Case Stud Therm Eng. 2022;40:102524.
- [42] Saeed A, Shah RA, Khan MS, Fernandez-Gamiz U, Bani-Fwaz MZ, Noeiaghdam S, et al. Theoretical analysis of unsteady squeezing nanofluid flow with physical properties. Math Biosci Eng. 2022;19(10):10176–91.
- [43] Jalili B, Ganji AD, Jalili P, Salman Nourazar S, Ganji DD. Thermal analysis of Williamson fluid flow with Lorentz force on the stretching plate. Case Stud Therm Eng. 2022;39:102374.
- [44] Ma Y, Mohebbi R, Rashidi MM, Yang Z, Sheremet MA. Numerical study of MHD nanofluid natural convection in a baffled U-shaped enclosure. Int J Heat Mass Transf. 2019;130:123–34.

- [45] Jalili B, Aghaee N, Jalili P, Domiri Ganji D. Novel usage of the curved rectangular fin on the heat transfer of a double-pipe heat exchanger with a nanofluid. Case Stud Therm Eng. 2022;35:102086.
- [46] Jalili P, Kazerani K, Jalili B, Ganji DD. Investigation of thermal analysis and pressure drop in non-continuous helical baffle with different helix angles and hybrid nano-particles. Case Stud Therm Eng. 2022;36:102209.
- [47] Dharmaiah G, Dinarvand S, Rama Prasad JL, Noeiaghdam S, Abdollahzadeh M. Non-homogeneous two-component buongiorno model for nanofluid flow toward Howarth's wavy cylinder with activation energy. Results Eng. 2023;17:100879.
- [48] Dharmaiah G, Dinarvand S, Durgaprasad P, Noeiaghdam S. Arrhenius activation energy of tangent hyperbolic nanofluid over a cone with radiation absorption. Results Eng. 2022:16:100745
- [49] Hosch WL. Navier-stokes equation. URL: https://www.britannica. com/science/Navier-Stokes-equation. (accessed: 20.04. 2018). 2018.

- [50] Talebi F, Mahmoudi AH, Shahi M. Numerical study of mixed convection flows in a square lid-driven cavity utilizing nanofluid. Int Commun Heat Mass Transf. 2010;37(1):79–90.
- [51] Loukopoulos VC, Tzirtzilakis EE. Biomagnetic channel flow in spatially varying magnetic field. Int J Eng Sci. 2004;42(5-6):571–90.
- [52] Sundar LS, Chandra Mouli KW, Said Z, Sousa ACM. Heat transfer and second law analysis of ethylene glycol-based ternary hybrid nanofluid under laminar flow. J Therm Sci Eng Appl. 2021;13(5):051021.
- [53] Yasmin A, Ali K, Ashraf M. MHD Casson nanofluid flow in a square enclosure with non-uniform heating using the Brinkman model. Eur Phys J Plus. 2021;136(2):1–14.
- [54] Shih T, Tan C, Hwang B. Effects of grid staggering on numerical schemes. Int | Numer Methods fluids. 1989;9(2):193–212.
- [55] Chen CL, Chang SC, Chen CK, Chang CK. Lattice Boltzmann simulation for mixed convection of nanofluids in a square enclosure. Appl Math Model. 2015;39(8):2436–51.
- [56] Davis GD. Natural-convection of air in a square cavity a bench-mark numerical-solution. Int J Numer Methods Fluids. 1983;3(3):249–64.